



Observations of the Crab Nebula and Pulsar with the Large-sized Telescope Prototype of the Cherenkov Telescope Array

H. Abe¹, K. Abe², S. Abe¹, A. Aguasca-Cabot³, I. Agudo⁴ , N. Alvarez Crespo⁵, L. A. Antonelli⁶ , C. Aramo⁷ , A. Arbet-Engels⁸, C. Arcaro⁹, M. Artero¹⁰ , K. Asano¹ , P. Aubert¹¹, A. Baktash¹² , A. Bamba¹³ , A. Baquero Larriva^{5,14} , L. Baroncelli¹⁵ , U. Barres de Almeida¹⁶ , J. A. Barrio⁵ , I. Batkovic⁹ , J. Baxter¹, J. Becerra González¹⁷ , E. Bernardini⁹ , M. I. Bernardos⁴, J. Bernete Medrano¹⁸, A. Berti⁸ , P. Bhattacharjee¹¹, N. Biederbeck¹⁹ , C. Bigongiari⁶ , E. Bissaldi²⁰ , O. Blanch¹⁰ , G. Bonnoli²¹, P. Bordas³ , A. Borghese²², A. Bulgarelli¹⁵ , I. Burelli²³, M. Buscemi²⁴ , M. Cardillo²⁵ , S. Caroff¹¹ , A. Carosi⁶ , F. Cassol²⁶ , D. Cauz²³, G. Ceribella¹, Y. Chai⁸ , K. Cheng¹, A. Chiavassa²⁷, M. Chikawa¹, L. Chytka²⁸, A. Cifuentes¹⁸, J. L. Contreras⁵ , J. Cortina¹⁸ , H. Costantini²⁶ , G. D'Amico²⁹, M. Dalchenko³⁰, A. De Angelis⁹ , M. de Bony de Lavergne¹¹ , B. De Lotto²³, R. de Menezes²⁷, G. Deleglise¹¹, C. Delgado¹⁸ , J. Delgado Mengual³¹ , D. della Volpe³⁰ , M. Dellaiera¹¹, D. Depaoli²⁷, A. Di Piano¹⁵, F. Di Piero²⁷ , R. Di Tria³², L. Di Venere³² , C. Díaz¹⁸ , R. M. Dominik¹⁹ , D. Dominis Prester³³ , A. Donini¹⁰ , D. Dorner³⁴ , M. Doró⁹ , D. Elsässer¹⁹ , G. Emery³⁰ , J. Escudero⁴ , V. Fallah Ramazani³⁵, G. Ferrara²⁴, F. Ferrarotto³⁶, A. Fiasson^{11,37} , L. Freixas Coromina¹⁸ , S. Fröse¹⁹, S. Fukami¹ , Y. Fukazawa³⁸ , E. Garcia¹¹ , R. Garcia López¹⁷ , C. Gasbarra³⁹, D. Gasparri³⁹ , F. Geyer¹⁹, J. Giesbrecht Paiva¹⁶, N. Giglietto²⁰ , F. Giordano³² , E. Giro⁹, P. Gliwny⁴⁰ , N. Godinovic⁴¹ , R. Grau¹⁰, D. Green⁸ , J. Green⁸ , S. Gunji⁴² , J. Hackfeld³⁵, D. Hadasch¹ , A. Hahn⁸ , K. Hashiyama¹, T. Hassan¹⁸ , K. Hayashi⁴³ , L. Heckmann⁸ , M. Heller³⁰ , J. Herrera Llorente¹⁷ , K. Hirotani¹ , D. Hoffmann²⁶ , D. Horns¹² , J. Houles²⁶ , M. Hrabovsky²⁸ , D. Hrupec⁴⁴ , D. Hui¹, M. Hütten¹ , M. Iarlori¹, R. Imazawa³⁸ , T. Inada¹ , Y. Inoue¹ , K. Ioka⁴⁶, M. Iori³⁶ , K. Ishio⁴⁰, Y. Iwamura¹, M. Jacquemont¹¹ , I. Jimenez Martinez¹⁸ , J. Jurysek⁴⁷ , M. Kagaya¹, V. Karas⁴⁸ , H. Katagiri⁴⁹ , J. Kataoka⁵⁰ , D. Kerszberg¹⁰ , Y. Kobayashi¹ , A. Kong¹ , H. Kubo¹ , J. Kushida² , M. Lainez⁵, G. Lamanna¹¹, A. Lamastra⁶ , T. Le Flour¹¹, M. Linhoff¹⁹ , F. Longo⁵¹ , R. López-Coto^{4,75} , M. López-Moya⁵ , A. López-Oramas¹⁷ , S. Loporchio³², A. Lorini⁵², P. L. Luque-Escamilla⁵³ , P. Majumdar^{1,54} , M. Makariev⁵⁵ , D. Mandat⁵⁶ , M. Manganaro³³ , G. Manico²⁴, K. Mannheim³⁴ , M. Mariotti⁹ , P. Marquez¹⁰ , G. Marsella^{24,57} , J. Martí⁵³ , O. Martínez⁵⁸ , G. Martínez¹⁸ , M. Martínez¹⁰ , P. Marusevec⁵⁹ , A. Mas-Aguilar⁵ , G. Maurin¹¹ , D. Mazin^{1,8} , E. Mestre Guillen¹⁷, S. Micanovic³³ , D. Miceli⁹ , T. Miener⁵ , J. M. Miranda⁵⁸ , R. Mirzoyan⁸ , T. Mizuno⁶⁰ , M. Molero Gonzalez¹⁷, E. Molina³ , T. Montaruli³⁰ , I. Monteiro¹¹, A. Moralejo¹⁰ , D. Morcuende^{4,5} , A. Morselli³⁹ , K. Mrakovic³, K. Murase¹ , A. Nagai³⁰, S. Nagataki⁶¹, T. Nakamori⁴² , L. Nickel¹⁹ , M. Nievas¹⁷ , K. Nishijima² , K. Noda¹ , D. Nosek⁶² , S. Nozaki⁸ , M. Ohishi¹ , Y. Ohtani¹ , T. Oka⁶³, N. Okazaki¹, A. Okumura^{64,65} , R. Orito⁶⁶, J. Otero-Santos¹⁷ , M. Palatiello²³ , D. Paneque⁸ , F. R. Pantaleo²⁰, R. Paoletti⁵² , J. M. Paredes³ , M. Pech^{28,56} , M. Pecimotika³³ , M. Peresano²⁷, A. Pérez⁵, E. Pietropaolo⁴⁵, G. Pirola⁸, C. Plard¹¹, F. Podobnik⁵², V. Poireau¹¹ , M. Polo¹⁸, E. Pons¹¹, E. Prandini⁹ , J. Prast¹¹ , G. Principe⁵¹, C. Priyadarshi¹⁰ , M. Prouza⁵⁶, R. Rando⁹ , W. Rhode¹⁹ , M. Ribó³ , V. Rizi⁴⁵ , G. Rodríguez Fernandez³⁹, J. E. Ruiz⁴, T. Saito¹ , S. Sakurai¹ , D. A. Sanchez¹¹, T. Šarić⁴¹ , Y. Sato⁶⁷, F. G. Saturni⁶ , B. Schleicher³⁴ , F. Schmuckermaier⁸, J. L. Schubert¹⁹, F. Schussler⁶⁸ , T. Schweizer⁸, M. Seglar Arroyo¹¹ , R. Silvia³², J. Sitarek⁴⁰ , V. Sliushar⁴⁷ , A. Spolon⁹ , J. Striškovíc⁴⁴ , M. Strzys¹ , Y. Suda³⁸ , Y. Sunada⁶⁹ , H. Tajima⁶⁴ , H. Takahashi³⁸, M. Takahashi¹ , J. Takata¹ , R. Takeishi¹ , P. H. T. Tam¹ , S. J. Tanaka⁶⁷ , D. Tateishi⁶⁹ , L. A. Tejedor⁵, P. Temnikov⁵⁵ , Y. Terada⁶⁹ , K. Terauchi⁶³, T. Terzić³³ , M. Teshima^{1,8}, M. Tluczykont¹², F. Tokanai⁴², D. F. Torres²² , P. Travnicek⁵⁶ , S. Truzzi⁵², A. Tutone⁶, G. Uhlrich³⁰, M. Vacula²⁸ , P. Vallania²⁷, J. van Scherpenberg⁸ , M. Vázquez Acosta¹⁷ , V. Verguilov⁵⁵ , I. Viale⁹ , A. Vigliano²³, C. F. Vignorito^{27,70} , V. Vitale³⁹ , G. Voutsinas³⁰, I. Vovk¹ , T. Vuillaume¹¹ , R. Walter⁴⁷, M. Will⁸ , T. Yamamoto⁷¹ , R. Yamazaki⁶⁷ , T. Yoshida⁴⁹ , T. Yoshikoshi¹ , N. Zywucka⁴⁰ , K. Bernlöhr⁷² , O. Gueta⁷³ , K. Kosack⁷⁴ , G. Maier⁷³ , and J. Watson⁷³

¹ Institute for Cosmic Ray Research, University of Tokyo, 5-1-5, Kashiwa-no-ha, Kashiwa, Chiba 277-8582, Japan² Department of Physics, Tokai University, 4-1-1, Kita-Kaname, Hiratsuka, Kanagawa 259-1292, Japan³ Departament de Física Quàntica i Astrofísica, Institut de Ciències del Cosmos, Universitat de Barcelona, IEEC-UB, Martí i Franquès, 1, E-08028, Barcelona, Spain⁴ Instituto de Astrofísica de Andalucía-CSIC, Glorieta de la Astronomía s/n, E-18008, Granada, Spain; lst-contact@cta-observatory.org⁵ IPARCOS-UCM, Instituto de Física de Partículas y del Cosmos, and EMFTTEL Department, Universidad Complutense de Madrid, E-28040 Madrid, Spain⁶ INAF—Osservatorio Astronomico di Roma, Via di Frascati 33, I-00040 Monteporzio Catone, Italy⁷ INFN Sezione di Napoli, Via Cintia, ed. G, I-80126 Napoli, Italy⁸ Max-Planck-Institut für Physik, Föhringer Ring 6, D-80805 München, Germany⁹ INFN Sezione di Padova and Università degli Studi di Padova, Via Marzolo 8, I-35131 Padova, Italy¹⁰ Institut de Física d'Altes Energies (IFAE), The Barcelona Institute of Science and Technology, Campus UAB, E-08193 Bellaterra (Barcelona), Spain¹¹ Univ. Savoie Mont Blanc, CNRS, Laboratoire d'Annecy de Physique des Particules—IN2P3, F-74000 Annecy, France¹² Universität Hamburg, Institut für Experimentalphysik, Luruper Chaussee 149, D-22761 Hamburg, Germany¹³ Graduate School of Science, University of Tokyo, 7-3-1 Hongo, Bunkyo-ku, Tokyo 113-0033, Japan¹⁴ Faculty of Science and Technology, Universidad del Azuay, Cuenca, Ecuador¹⁵ INAF—Osservatorio di Astrofisica e Scienza dello spazio di Bologna, Via Piero Gobetti 93/3, I-40129 Bologna, Italy¹⁶ Centro Brasileiro de Pesquisas Físicas, Rua Xavier Sigaud 150, RJ 22290-180, Rio de Janeiro, Brazil¹⁷ Instituto de Astrofísica de Canarias and Departamento de Astrofísica, Universidad de La Laguna, La Laguna, Tenerife, Spain¹⁸ CIEMAT, Avda. Complutense 40, E-28040 Madrid, Spain

- ¹⁹ Department of Physics, TU Dortmund University, Otto-Hahn-Str. 4, D-44227 Dortmund, Germany
- ²⁰ INFN Sezione di Bari and Politecnico di Bari, via Orabona 4, I-70124 Bari, Italy
- ²¹ INFN—Osservatorio Astronomico di Brera, Via Brera 28, I-20121 Milano, Italy
- ²² Institute of Space Sciences (ICE, CSIC), and Institut d’Estudis Espacials de Catalunya (IEEC), and Institució Catalana de Recerca i Estudis Avançats (ICREA), Campus UAB, Carrer de Can Magrans, s/n E-08193 Bellaterra, Spain
- ²³ INFN Sezione di Trieste and Università degli studi di Udine, via delle scienze 206, I-33100 Udine, Italy
- ²⁴ INFN Sezione di Catania, Via S. Sofia 64, I-95123 Catania, Italy
- ²⁵ INFN—Istituto di Astrofisica e Planetologia Spaziali (IAPS), Via del Fosso del Cavaliere 100, I-00133 Roma, Italy
- ²⁶ Aix Marseille Univ, CNRS/IN2P3, CPPM, Marseille, France
- ²⁷ INFN Sezione di Torino, Via P. Giuria 1, I-10125 Torino, Italy
- ²⁸ Palacky University Olomouc, Faculty of Science, 17. listopadu 1192/12, 771 46 Olomouc, Czech Republic
- ²⁹ Department of Physics and Technology, University of Bergen, Muselass 1, 5007 Bergen, Norway
- ³⁰ University of Geneva—Département de physique nucléaire et corpusculaire, 24 Quai Ernest Ansermet, 1211 Genève 4, Switzerland
- ³¹ Port d’Informació Científica, Edifici D, Carrer de l’Albareda, E-08193 Bellaterra (Cerdanyola del Vallès), Spain
- ³² INFN Sezione di Bari and Università di Bari, via Orabona 4, I-70126 Bari, Italy
- ³³ University of Rijeka, Department of Physics, Radmile Matejcic 2, 51000 Rijeka, Croatia
- ³⁴ Institute for Theoretical Physics and Astrophysics, Universität Würzburg, Campus Hubland Nord, Emil-Fischer-Str. 31, D-97074 Würzburg, Germany
- ³⁵ Institut für Theoretische Physik, Lehrstuhl IV: Plasma-Astroteilchenphysik, Ruhr-Universität Bochum, Universitätsstraße 150, D-44801 Bochum, Germany
- ³⁶ INFN Sezione di Roma La Sapienza, P.le Aldo Moro, 2, I-00185 Rome, Italy
- ³⁷ ILANCE, CNRS—University of Tokyo International Research Laboratory, Kashiwa, Chiba 277-8582, Japan
- ³⁸ Physics Program, Graduate School of Advanced Science and Engineering, Hiroshima University, 739-8526 Hiroshima, Japan
- ³⁹ INFN Sezione di Roma Tor Vergata, Via della Ricerca Scientifica 1, I-00133 Rome, Italy
- ⁴⁰ Faculty of Physics and Applied Informatics, University of Lodz, ul. Pomorska 149-153, 90-236 Lodz, Poland
- ⁴¹ University of Split, FESB, R. Boškovića 32, 21000 Split, Croatia
- ⁴² Department of Physics, Yamagata University, Yamagata, Yamagata 990-8560, Japan
- ⁴³ Tohoku University, Astronomical Institute, Aobaku, Sendai 980-8578, Japan
- ⁴⁴ Josip Juraj Strossmayer University of Osijek, Department of Physics, Trg Ljudevita Gaja 6, 31000 Osijek, Croatia
- ⁴⁵ INFN Dipartimento di Scienze Fisiche e Chimiche—Università degli Studi dell’Aquila and Gran Sasso Science Institute, Via Vetoio 1, Viale Crispi 7, I-67100 L’Aquila, Italy
- ⁴⁶ Kitashirakawa Oiwakecho, Sakyo Ward, Kyoto, 606-8502, Japan
- ⁴⁷ Department of Astronomy, University of Geneva, Chemin d’Ecogia 16, CH-1290 Versoix, Switzerland
- ⁴⁸ Astronomical Institute of the Czech Academy of Sciences, Bocni II 1401-14100 Prague, Czech Republic
- ⁴⁹ Faculty of Science, Ibaraki University, Mito, Ibaraki, 310-8512, Japan
- ⁵⁰ Faculty of Science and Engineering, Waseda University, Shinjuku, Tokyo 169-8555, Japan
- ⁵¹ INFN Sezione di Trieste and Università degli Studi di Trieste, Via Valerio 2, I-34127 Trieste, Italy
- ⁵² INFN and Università degli Studi di Siena, Dipartimento di Scienze Fisiche, della Terra e dell’Ambiente (DSFTA), Sezione di Fisica, Via Roma 56, I-53100 Siena, Italy
- ⁵³ Escuela Politécnica Superior de Jaén, Universidad de Jaén, Campus Las Lagunillas s/n, Edif. A3, E-23071 Jaén, Spain
- ⁵⁴ Saha Institute of Nuclear Physics, Bidhannagar, Kolkata-700 064, India
- ⁵⁵ Institute for Nuclear Research and Nuclear Energy, Bulgarian Academy of Sciences, 72 boul. Tsarigradsko chaussee, 1784 Sofia, Bulgaria
- ⁵⁶ FZU—Institute of Physics of the Czech Academy of Sciences, Na Slovance 1999/2, 182 21 Praha 8, Czech Republic
- ⁵⁷ Dipartimento di Fisica e Chimica ‘E. Segrè’ Università degli Studi di Palermo, via delle Scienze, 90128 Palermo
- ⁵⁸ Grupo de Electronica, Universidad Complutense de Madrid, Av. Complutense s/n, E-28040 Madrid, Spain
- ⁵⁹ Department of Applied Physics, University of Zagreb, Horvatovac 102a, 10000 Zagreb, Croatia
- ⁶⁰ Hiroshima Astrophysical Science Center, Hiroshima University, Higashi-Hiroshima, Hiroshima 739-8526, Japan
- ⁶¹ RIKEN, Institute of Physical and Chemical Research, 2-1 Hirosawa, Wako, Saitama, 351-0198, Japan
- ⁶² Charles University, Institute of Particle and Nuclear Physics, V Holešovičkách 2, 180 00 Prague 8, Czech Republic
- ⁶³ Division of Physics and Astronomy, Graduate School of Science, Kyoto University, Sakyo-ku, Kyoto, 606-8502, Japan
- ⁶⁴ Institute for Space-Earth Environmental Research, Nagoya University, Chikusa-ku, Nagoya 464-8601, Japan
- ⁶⁵ Kobayashi-Maskawa Institute (KMI) for the Origin of Particles and the Universe, Nagoya University, Chikusa-ku, Nagoya 464-8602, Japan
- ⁶⁶ Graduate School of Technology, Industrial and Social Sciences, Tokushima University, Tokushima 770-8506, Japan
- ⁶⁷ Department of Physical Sciences, Aoyama Gakuin University, Fuchinobe, Sagami-hara, Kanagawa, 252-5258, Japan
- ⁶⁸ IRFU, CEA, Université Paris-Saclay, Bât 141, F-91191 Gif-sur-Yvette, France
- ⁶⁹ Graduate School of Science and Engineering, Saitama University, 255 Simo-Ohkubo, Sakura-ku, Saitama city, Saitama 338-8570, Japan
- ⁷⁰ Dipartimento di Fisica—Università degli Studi di Torino, Via Pietro Giuria 1, I-10125 Torino, Italy
- ⁷¹ Department of Physics, Konan University, Kobe, Hyogo, 658-8501, Japan
- ⁷² Max-Planck-Institut für Kernphysik, P.O. Box 103980, D-69029 Heidelberg, Germany
- ⁷³ Deutsches Elektronen-Synchrotron, Platanenallee 6, D-15738 Zeuthen, Germany
- ⁷⁴ CEA/IRFU/Sap, CEA Saclay, Bat 709, Orme des Merisiers, F-91191 Gif-sur-Yvette, France

Received 2023 April 21; revised 2023 June 22; accepted 2023 July 14; published 2023 October 10

Abstract

The Cherenkov Telescope Array (CTA) is a next-generation ground-based observatory for gamma-ray astronomy at very high energies. The Large-Sized Telescope prototype (LST-1) is located at the CTA-North site, on the Canary Island of La Palma. LSTs are designed to provide optimal performance in the lowest part of the energy

⁷⁵ Corresponding authors: R. López-Coto, A. Moralejo, D. Morcuende, S. Nozaki, and T. Vuillaume.



range covered by CTA, down to $\simeq 20$ GeV. LST-1 started performing astronomical observations in 2019 November, during its commissioning phase, and it has been taking data ever since. We present the first LST-1 observations of the Crab Nebula, the standard candle of very-high-energy gamma-ray astronomy, and use them, together with simulations, to assess the performance of the telescope. LST-1 has reached the expected performance during its commissioning period—only a minor adjustment of the preexisting simulations was needed to match the telescope’s behavior. The energy threshold at trigger level is around 20 GeV, rising to $\simeq 30$ GeV after data analysis. Performance parameters depend strongly on energy, and on the strength of the gamma-ray selection cuts in the analysis: angular resolution ranges from $0^\circ.12$ – $0^\circ.40$, and energy resolution from 15%–50%. Flux sensitivity is around 1.1% of the Crab Nebula flux above 250 GeV for a 50 hr observation (12% for 30 minutes). The spectral energy distribution (in the 0.03–30 TeV range) and the light curve obtained for the Crab Nebula agree with previous measurements, considering statistical and systematic uncertainties. A clear periodic signal is also detected from the pulsar at the center of the Nebula.

Unified Astronomy Thesaurus concepts: [Gamma-ray astronomy \(628\)](#); [Gamma-ray sources \(633\)](#); [Astronomy data analysis \(1858\)](#); [Pulsar wind nebulae \(2215\)](#); [Pulsars \(1306\)](#)

1. Introduction

Astronomical observations across the electromagnetic spectrum span more than 20 decades in photon energy, requiring the use of a wide range of instrumental techniques. At the high-energy end of the spectrum, in the so-called very-high-energy (VHE) gamma-ray band and above ($E_\gamma \gtrsim 50$ GeV), photons are scarce, and the performance of space-borne facilities is limited by their modest photon collection areas. Ground-based instruments (Sitarek 2022), on the other hand, can achieve much larger effective areas by exploiting the effects of the absorption in the atmosphere of a VHE photon: the development of an extensive air shower (EAS) of secondary particles. Imaging Atmospheric Cherenkov Telescopes (IACTs) collect the Cherenkov light produced by the ultrarelativistic EAS particles (mostly electrons and positrons), and form an image of the shower, from which the direction and energy of the primary photon can be estimated.

The Crab Nebula was the first source detected in the VHE sky (Weekes et al. 1989), now featuring around 250 known objects (Sitarek 2022). The Crab Pulsar Wind Nebula is the remnant of a supernova explosion observed in 1054 A.D. It is one of the most studied objects in the sky (Hester 2008; Bühler & Blandford 2014), and its spectrum extends from radio up to petaelectronvolt gamma rays (LHAASO Collaboration et al. 2021). Flaring or flickering behavior has been reported below a few giga-electronvolts (Abdo et al. 2011), but in the VHE band it remains a steady source (Aliu et al. 2014; H.E.S.S. Collaboration et al. 2014), and is currently the standard candle used by different instruments (Aharonian et al. 2006; Aleksić et al. 2015).

The Cherenkov Telescope Array⁷⁶ (CTA) is a next-generation ground-based observatory for VHE gamma-ray astronomy. CTA will consist of two arrays of IACTs of different sizes deployed on two sites: one in the Northern Hemisphere, in the Roque de los Muchachos Observatory (ORM) in the Canary Island of La Palma, and another one in the Southern Hemisphere, in the Atacama desert in Chile. The largest among the CTA telescopes are the Large-Sized Telescopes⁷⁷ (LSTs; Cortina 2019), four of which will be part of the CTA-North array. LSTs are equipped with 23 m diameter mirror dishes, which enable them to detect the faint Cherenkov flashes from showers initiated by gamma rays down to $\simeq 20$ GeV. The lightweight LST structure is designed to allow

for fast slewing, and hence facilitate follow-up observations of transients. LST-1, the prototype of the LST, was inaugurated at the ORM in 2018 October and has been taking science data since 2019 November.

This paper presents observations of the Crab Nebula performed with LST-1 between 2020 November and 2022 March, while the telescope was still in its commissioning phase. These observations are used to characterize the performance of the instrument, and to validate the Monte Carlo (MC) simulations needed for the data analysis. Section 2 describes the MC simulations. The data analysis pipeline is summarized in Section 3, which also presents some key LST-1 performance parameters (energy and angular resolution) as determined from the MC. Section 4 introduces the Crab Nebula data sample, which in Section 5 is used to verify the validity of the simulations. Section 6 presents the results on the Crab Nebula spectrum and light curve, and an estimate of the LST-1 sensitivity, and finally we provide conclusions in Section 7

2. Monte Carlo Simulations

An IACT uses the atmosphere as a key element in the detection process; hence, there is obviously no way to characterize its end-to-end response in a controlled setup (unlike space-borne gamma-ray telescopes, which can be beam-tested in the lab prior to launch). The analysis of IACT images to reconstruct the properties of the shower primary (particle identity, energy, and direction) relies heavily on detailed MC simulations both of the shower development and of the telescope. The simulated events, for which we know the true attributes of the primary particle, will allow us to train the event reconstruction algorithms to be used on the real data. The same algorithms are also applied to an independent MC sample (“test” sample), from which the instrument response functions (IRFs) can be derived.

2.1. General Description

We simulate the shower development in the atmosphere, and the Cherenkov light emission and propagation, using CORSIKA v7.7100 (Heck et al. 1998). For the telescope simulation, we use `sim_telarray` v2020-06-28 (Bernlöhr 2008). The telescope simulation includes the reflection of the Cherenkov light on the mirror dish, its passage through the camera entrance window, and its detection on the focal plane equipped with light concentrators and photomultiplier tubes (PMTs). All of the stages are simulated taking into account the

⁷⁶ <https://www.cta-observatory.org/>

⁷⁷ <https://www.lst1.iac.es/>

lab-measured performance of the different telescope elements as a function of the photon wavelength and, when relevant, its incident direction. The camera trigger system, the electronic chain for the signal processing, and the digitization of the analog signals are also simulated in detail to obtain digital waveforms (two per pixel, from a high- and a low-gain branch) completely equivalent to those present in the real LST-1 data after the correction of low-level features of the data acquisition electronics (see Section 3.1). From this point onward, the same analysis pipeline, described in Section 3, can be applied to simulated and observed data.

To train the event reconstruction algorithms (training MC sample), we use simulations of two types of primary particles: gamma rays and protons. To evaluate the response of the telescope (test MC sample), we only simulate gamma rays. For the analysis of gamma-ray observations, it is not strictly necessary to obtain from MC simulations the response of the telescope to background events (showers initiated by electrons, protons, and heavier cosmic-ray nuclei). The precise simulation of the background of an IACT is challenging, due to the uncertainties in the hadronic interaction models (see, e.g., Ohishi et al. 2021) and in the cosmic-ray composition, but, as we will see, a reliable estimation of the background event rates recorded from the direction of the source of interest can be obtained using a control (off-source) sky region, i.e., using simple aperture photometry. Finally, we also produce simulations of single muons, which are helpful to evaluate the overall optical efficiency of the telescope (Gaug et al. 2019). The main simulation parameters for the production of each type of primary are presented below.

2.2. MC Generation Limits

2.2.1. Gamma Rays

Gamma rays are simulated with a differential energy spectrum $dN/dE \propto E^{-2}$. For vertical incidence, the energy range was set to 5 GeV–50 TeV. In order to account for the variation of the telescope energy threshold with the zenith distance (ZD), these energy limits are then modified as $E_{\min, \max} \propto \cos^{-2.5}(\text{ZD})$, with a maximum value of 200 TeV.

In the training sample, the directions of the gamma rays are distributed isotropically around the telescope pointing up to an offset angle of 2.5° , such that the event reconstruction algorithms can be trained (see Section 3.3) to perform well for sources anywhere in the field of view. In order to speed up the simulations, and considering the low global trigger efficiency, each generated shower is used 10 times, placing the telescope at 10 different random locations around the shower axis, out to a maximum impact parameter of 900 m for $\text{ZD} = 0$. This value is scaled as $\cos^{-0.5}(\text{ZD})$ for larger ZDs.

The gamma-ray test sample is produced in a similar way; although, for the analysis of standard observations of pointlike sources, in which the telescope is pointed at a sky position 0.4° away from the source (see Section 4), the gamma-ray directions are all generated with that precise offset from the telescope pointing (in random orientations). The small offset angle allows us to reduce the maximum impact to 700 m for vertical incidence, which is then scaled as $\cos^{-1}(\text{ZD})$.

From the dependence of the air mass as $\cos^{-1}(\text{ZD})$ in the plane-parallel approximation, one would naively expect (for electromagnetic showers and in absence of atmospheric absorption) the same evolution of the distance to the shower

maximum, and hence of the radius of the Cherenkov light pool. The photon density reaching the mirror dish would change as $\cos^2(\text{ZD})$ under the same assumptions. This would suggest using $\cos^{-2}(\text{ZD})$ and $\cos^{-1}(\text{ZD})$ scalings for the energy generation limits and the maximum impact parameter, respectively. These simple zenith-scaling laws were re-evaluated empirically using an earlier simulation library with protons and gamma rays simulated at ZDs of 20° , 40° , and 60° . The power index for the energy generation limits was corrected to -2.5 (a faster increase with zenith) to keep the fraction of triggers (and hence the computational cost of producing triggered events) closer to the one at zenith. As for the maximum impact parameter, the $\cos^{-1}(\text{ZD})$ dependence worked well for the gamma-ray test sample, whereas $\cos^{-0.5}(\text{ZD})$ (a slower increase) was chosen for the diffuse gamma simulations (training sample), to moderate the drop in the production efficiency.

2.2.2. Protons

Protons for the training sample are generated following the same scaling of maximum impact parameter and energy range as for diffuse gamma rays. The energy range for vertical incidence is 10 GeV–100 TeV (taking into account their lower Cherenkov light yield compared to gamma rays of the same energy), and the maximum energy is also capped at 200 TeV. The maximum impact parameter is 1500 m for vertical showers, and the number of shower reuses is also set at 10. Directions are isotropically distributed within 8° of the telescope pointing, with that maximum offset changing as $\cos^{0.5}(\text{ZD})$ —once again, a dependence obtained empirically to maintain a production efficiency similar to that at zenith. For hadronic showers, as compared to electromagnetic ones, it is harder to estimate zenith-dependent optimal production ranges from simple arguments, due to the production of electromagnetic subshowers and muons at large angles relative to the primary particle.

The MC production ranges and zenith-scaling laws above may be revised in the near future to further reduce the computational cost of the MC generation. Note that we do not need a “complete” MC proton training sample, in the sense of containing all (or a very large fraction of all) of the protons that would trigger the telescope. Its only purpose is to be used in the training of the particle classification algorithm together with the gamma rays, and this can be achieved as long as the simulated protons produce a sufficiently representative sample of the hadronic shower images that the real background (protons and other nuclei) will generate. On the other hand, we cannot exclude that a *more complete* training sample (more computationally expensive) could bring some improvement to the performance we present in this paper.

2.2.3. Muons

Single muons are simulated with a power-law differential energy spectrum with index -2.0 , between 8.4 GeV and 1 TeV. The maximum impact parameter is 9.8 m, corresponding to 80% of the mirror radius, since we are interested in muons that produce large rings on the camera. The maximum off-axis angle is 0.9° , which means the rings would be fully contained on the camera. Muons are simulated with vertical incidence. The amount of Cherenkov light produced by a single muon and collected by the telescope correlates very well with its impact

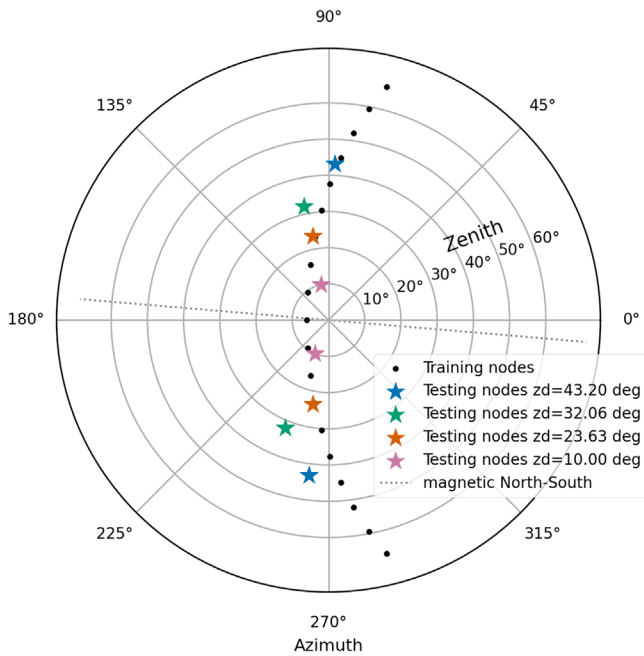


Figure 1. Pointing directions of the nodes. The training nodes are used to train the shower reconstruction algorithms. The testing nodes are used to compute the IRFs from point-source gamma-ray simulations. The nodes that have the same altitude and symmetrical azimuths with respect to the magnetic north are combined (by color here) to compute the IRFs in Figure 7.

parameter, direction of incidence, and Cherenkov emission angle (which in turn depends on its energy). All of these parameters can be reconstructed from the ring-shaped image formed on the camera, which makes isolated muons a perfect tool for the calibration of the total light throughput of the telescope (Gaug et al. 2019). This is achieved through comparison of the actual observations with muon simulations performed with different global optical efficiency of the telescope. For the present work, we simulated 10^4 muons per optical efficiency, which we vary in steps of 10%.

2.3. MC Pointing Grids

Simulations of gamma rays and protons were performed in a wide range of telescope pointing directions, up to $\approx 70^\circ$ ZD. These directions were chosen in two different grids of pointings, one for the training MC and one for the test MC.

2.3.1. Training MC

The training MC is simulated using pointings along “decl. lines,” i.e., following the trajectory in horizontal (Alt-Az) coordinates that all sources at a given decl. follow as viewed from the LST-1 site. We simulated 15 different decl. lines (from -29° to $+67^\circ$, distributed in steps of $\cos(\text{ZD}_{\min})$, where ZD_{\min} is the zenith angle at culmination. In each line, around 20 different pointings equally spaced in hour angle are defined, with the limits being determined as: $\text{ZD} < 70^\circ$ and ± 6 hr around culmination. For the analysis of the Crab Nebula observations presented here, we used the closest decl. line, which corresponds to culmination at $\text{ZD} = 6^\circ$ (i.e., $\delta = 22^\circ 76'$), and has a total of 19 pointings; see Figure 1. The rationale behind this grid design is to train the algorithms with the MC from all directions along the chosen decl. line, including the telescope (Alt-Az) pointing coordinates among the parameters made available as input to the reconstruction (see Section 3.3).

In this way, the algorithms can automatically *learn* how image parameters vary with the incidence direction of the shower primary (mainly through the variations of air mass with ZD). In principle, one could also train the algorithms with “all-sky” simulations, i.e., the full grid of pointings, and obtain algorithms that would be able to reconstruct events from any direction, regardless of the sky coordinates of the observed source. However, this would result in algorithms with significantly higher memory needs (for our decl.-wise approach, the size of the four random forests is already 18.1 GB, which have to be kept in memory during the analysis), and no improvement in performance, since the analysis of any given source would only make use of the pointings along the source path.

2.3.2. Test MC

The test MC is simulated in a grid of zenith and azimuth values. For a single IACT, the relevant direction-dependent quantities that affect the performance are the air mass (which increases like $1 / \cos(\text{ZD})$ in the planar atmosphere approximation) and the component of the geomagnetic field orthogonal to the shower axis (which is the relevant one affecting the shower shape, via the Lorentz force acting on the secondary charged particles). We therefore produced a regular triangular grid in $\cos(\text{ZD})$ and B_\perp/B . Eventually we will use this test MC grid to calculate the IRFs in each node, and then interpolate them to obtain the IRFs for any arbitrary telescope pointing, but this procedure is still in development; for the present analysis, we will simply use for each data run the IRFs obtained with the closest test MC grid node. Two nodes at $\text{ZD} = 10^\circ$ and two nodes at $\text{ZD} = 32^\circ$ from the regular grid have been used in this work for the analysis of observations within 35° of zenith. Additionally, we also used an MC generated for two additional pointings at $\text{ZD} = 23^\circ 6'$ (along the Crab path, on both sides of culmination) to improve the precision of the IRFs, considering that we are using no interpolation to the actual telescope orientation. Figure 1 shows all pointing directions in our test MC sample.

2.4. Adjustments of the MC Telescope Simulation

The MC simulation of the Cherenkov light detection is initially based on lab measurements of the individual response of the different telescope elements (e.g., the reflectivity of the mirrors, or the photon detection efficiency of the PMTs). Typically, the simulation parameters need some tuning in order to match the overall performance of the telescope once deployed on site, where it is subject to various sources of degradation (dirt on mirrors or on the camera window, varying atmospheric conditions, different levels of background light, temporarily misaligned mirror tiles, etc.). Below we describe the adjustments performed on the LST-1 MC simulation for the analysis of the data taken during the commissioning period.

2.4.1. Optical Efficiency

The overall optical efficiency of an IACT can be affected by mirror degradation or dust deposit on its surface, which would reduce its reflectivity. The optical efficiency in the MC is tuned to the real optical efficiency of the telescope obtained through the analysis of muon rings (Gaug et al. 2019). We monitor this optical efficiency in the daily data checks to spot possible problems such as misaligned mirrors, or loss of reflectivity. The

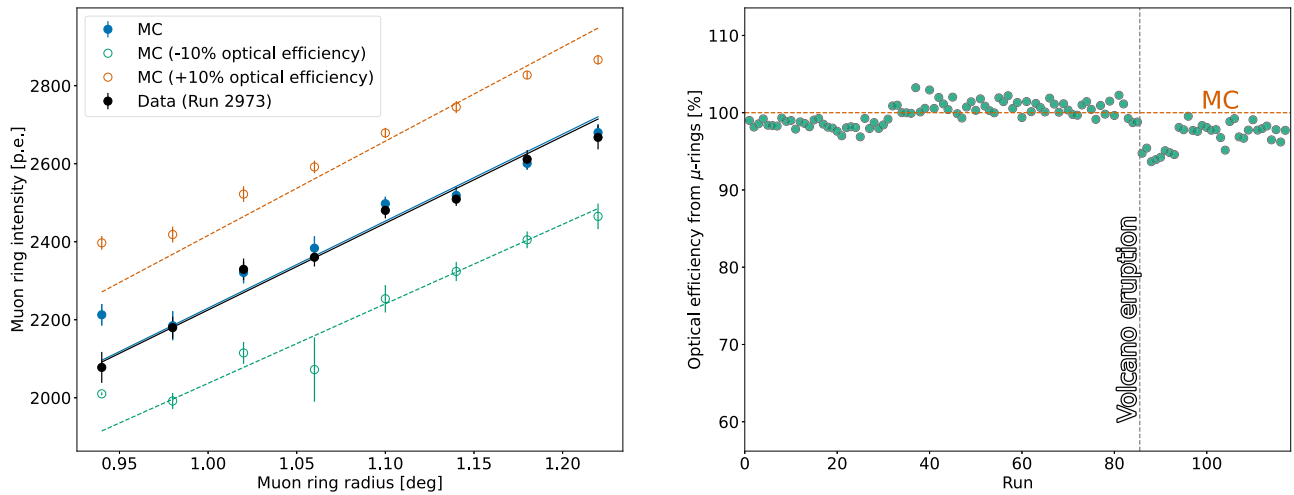


Figure 2. Left panel: total light in muon rings detected by LST-1 vs. ring radius. Data from one run is compared to three different simulations, with telescope efficiency changing in steps of 10%. Right panel: run-wise LST-1 optical efficiency derived using muon ring intensity, for the sample of good-quality Crab Nebula observations analyzed in this work. The vertical dashed line separates the runs taken before and after the volcanic eruption in La Palma (which took place between 2021 September 19 and December 13). The observed variations are mostly driven by changes in the number of correctly aligned mirrors, and in their reflectivity. For example, the early post-eruption data indicated a $\simeq 5\%$ lower efficiency, which partially recovered after some rainfall in 2022 February, which presumably removed dirt from the dish surface.

method works as follows: for muon rings (unlike for shower images; see Section 3.1) we obtain the pixel-wise charges with an unbiased pulse integrator, i.e., one with a common integration time window for all pixels, defined around the camera-averaged peak time of the muon light pulse. Pixels not illuminated by the muon, containing only noise, will on average have zero charge—the unbiased integrator will not pick preferentially positive fluctuations of the night sky background (NSB) light. Then a fit is performed to obtain the geometrical ring parameters (center and radius R). The total light (or muon ring intensity) is obtained by adding up the charges in all pixels whose centers are at a distance between $0.75R$ and $1.25R$ from the ring center. This integration range is large enough to contain all of the muon light, considering the optical point-spread function (PSF) of the telescope, and the possible inaccuracies of the ring fit. The muon ring intensity is expected to be proportional to the muon ring radius (which is the Cherenkov angle of the muon); see Equation (21) of Gaug et al. (2019). The left panel of Figure 2 shows this approximate behavior for the rings recorded in one LST-1 data run, compared to MC simulations with three different efficiencies.

The optical efficiency of the telescope may fluctuate on a nightly basis at the few percent level, as can be seen in the right panel of Figure 2, which shows its evolution as measured from well-contained muon rings in the sample of 117 good-quality Crab observation runs (of a typical duration of 20 minutes) spanning $\simeq 1.5$ yr, which will be described in Section 4. Given the small variations of the muon light yield, for the analysis presented in this paper, no run-wise tuning has been introduced; a single optical efficiency (indicated as “100%” in Figure 2) was used in the MC simulations used for the analysis of the whole data sample.

2.4.2. Optical Point-spread Function

The optical PSF of the LST-1 mirror dish is measured by a dedicated CCD camera located at its center, which records images of stars focused on a special removable screen located between the focal plane and the camera entrance window. The

simulation can be tuned to match the real PSF through two parameters, which determine the spread in the orientations of the individual mirror tiles relative to their ideal alignment. The quality of the PSF of the telescope may fluctuate due to, e.g., sporadic problems in the active mirror control system, but in the period considered in this work, no significant variations were recorded that would require separate MCs with different adjustments. Therefore, for the analysis presented in this paper, the same PSF was used in the MC simulations of the telescope. With the selected settings, 80% of the PSF is contained in a circle with a diameter of $\simeq 0^{\circ}06$, i.e., well within one pixel ($\odot = 0^{\circ}1$).

2.4.3. Night Sky Background

In the LST-1 simulations with `sim_telarray` the assumed level of NSB light is that of a “dark” sky field (typical of observations away from the Galactic disk and the zodiacal plane). It results in an average photoelectron (p.e.) rate of 193 MHz per pixel.

LST-1 observations, on the other hand, are performed in a wide range of NSB conditions (even with the Moon above the horizon). Instead of re-running the telescope simulation for different levels of NSB, which would be computationally expensive, we adopt the approach known as “noise padding,” which consists of adding some random Poissonian noise during the analysis of the MC events (right before the image cleaning—see Section 3), to match the average NSB level in the data. The level of NSB in a given field of view is measured using the interleaved pedestal events acquired during observations at a rate of 100 Hz (these are events containing only noise). Since all of the data analyzed in this work were recorded in dark-night conditions (with the Moon below the horizon), and pointing toward the same sky region, the whole sample can be processed with a single NSB tuning of the MC (which corresponds to an $\simeq 70\%$ larger NSB p.e. rate than the default in the simulation).

3. Pipeline Description

`cta-lstchain` (Lopez-Coto et al. 2022) is the data analysis pipeline used to process the LST-1 data. It is heavily based on `ctapipe` (Kosack et al. 2021; Nöthe et al. 2022), the prototype low-level analysis framework of CTA. `cta-lstchain` uses the `ctapipe_io_lst`⁷⁸ plug-in to read in the raw data files, and to apply a first calibration to the camera signals. `cta-lstchain` performs the event reconstruction as described below, and outputs files containing lists of gamma-ray candidate events (including event-wise reconstructed parameters like energy and incoming direction) writing out DL3 data in the format specified by the Data Formats for Gamma-Ray Astronomy (GADR; Deil et al. 2018; Nigro et al. 2019). These files can be further processed with `Gammapy` (Deil et al. 2017; Donath et al. 2022), the official high-level data analysis framework of CTA, to obtain final analysis products like energy spectra or light curves. The IRFs accompanying the selected gamma-ray candidate events in the DL3 files are produced using `pyirf` (Nöthe et al. 2022). Most of the data reduction was carried out in an on-site computing infrastructure at La Palma using `lstosa` (Morcuende et al. 2022; Ruiz et al. 2022), a library that automatizes the processing of the LST-1 data through the `cta-lstchain` pipeline.

In the rest of this section we provide details on the different stages of the event reconstruction carried out by `cta-lstchain`.

3.1. Pixel-wise Charge Integration

For every triggered event, the raw data recorded by the LST-1 camera consists of 12-bit digitized waveforms. Two such waveforms (corresponding to the high- and low-gain branches) are stored per pixel, each having 40 samples taken at 1 ns intervals. The raw waveforms are calibrated as described in Kobayashi et al. (2022). In most cases, the calibrated high-gain waveform is that used for further analysis; only when it has one or more raw samples above 3500 counts is the high gain discarded and the low gain is used instead (the transition occurs at a charge of around 200 p.e. per pixel). Each waveform is then integrated in an 8-sample range (1 sample \simeq 1 ns), using the so-called `LocalPeakWindowSum` algorithm, in the range $[s_{\max} - 3, s_{\max} + 4]$, where s_{\max} is the sample with the highest value in the calibrated waveform. The integrated charge is converted to photoelectrons using conversion factors determined (using the so-called F-factor method) in the analysis of dedicated calibration runs (Kobayashi et al. 2022). The conversion factors include a correction for the (average) pulse tails beyond the integration window, which typically contains around 84% of the total charge. In addition to the integrated charge, for each pixel we calculate a signal arrival time using a simple charge-weighted average of the sample times.

3.2. Image Cleaning and Parameterization

The vast majority of pixels in each camera event contain only noise, fluctuations of the NSB light. A procedure called “image cleaning” is applied to each event to select the pixels that contain a significant amount of Cherenkov light from the shower. Two charge thresholds are defined, with default values 8 and 4 p.e.—known as “picture” and “boundary” thresholds,

respectively (Lessard et al. 2001). A first pixel selection is performed applying the following algorithm:

- (i) increase the picture threshold for pixels that have a large level of noise: we will replace the default value by $\langle Q_{\text{ped}} \rangle + 2.5 \cdot \sigma_{Q_{\text{ped}}}$, if that value happens to be larger than the default 8 p.e. The quantities $\langle Q_{\text{ped}} \rangle$ and $\sigma_{Q_{\text{ped}}}$ are the mean and the standard deviation of the reconstructed charge of that specific pixel, as computed from interleaved pedestal events.
- (ii) select pixels with charge above the picture threshold, and with at least two neighboring pixels above the picture threshold. The pixels fulfilling this condition form the “core” of the image.
- (iii) select pixels with charge above the boundary threshold and at least one core neighbor.

We then apply the following additional conditions to keep a pixel as part of the final image:

- (iv) to have at least one neighbor (among the preselected set of pixels described above) with signal arrival time within 2 ns of its own arrival time.
- (v) to have a charge above $0.03 \cdot Q_{\text{peak}}$, where Q_{peak} is the average charge of the three brightest pixels in the image.

A convenient way of assessing the effectiveness of the image cleaning algorithm is to check the probability that a pedestal event survives the procedure (i.e., it has a nonzero number of surviving pixels). That probability will be the same with which spurious islands of noise-only events survive the cleaning in the analysis of genuine shower images. Such noise-only islands have the potential of spoiling the shower reconstruction. Conditions (i)–(iv) are sufficient, for observations with LST-1 in dark conditions (with the Moon below the horizon), to have a fraction $< O(10^{-3})$ of cleaning-surviving pedestal events.

Step (i) is necessary in order to ensure that bright stars in the field of view (which increase in the illuminated pixels the rate of signals above the default picture threshold) do not produce a significant number of spurious islands. The values of $\langle Q_{\text{ped}} \rangle$ and $\sigma_{Q_{\text{ped}}}$ are calculated every few seconds using interleaved pedestal events, to take into account the rotation of the star field during an observation. This “antistar” condition will increase the effective cleaning threshold in the pixels around stars, and in turn produce a deficit of dim images in those areas, i.e., a nonuniformity in the response of the camera at low energies. In order to limit this effect, it is important that the *default* picture threshold is high enough so that only a small part of the camera pixels get their picture thresholds modified in step (i). In this way we will still be able to use for the subsequent analysis a simplified MC simulation with a uniform NSB level across the field of view (and hence uniform camera response). For the default picture threshold of 8 p.e., and the sample analyzed in this paper, only 4.7% of the camera pixels (on average) end up with increased values due to the effect of stars (and only 1.2% have a value above 10 p.e.).

Conditions (ii), (iii), and (iv) are intended to select groups of neighboring pixels with significant signals arriving close in time, as expected for showers (and reject noise fluctuations, which are not correlated in different pixels). Condition (v) is introduced to solve a problem present in some of the LST-1 data taken in the commissioning phase: occasionally some mirror tiles were purposefully misaligned (making them point $\simeq 2^\circ$ away from the main spot), whenever they could not be

⁷⁸ https://github.com/cta-observatory/ctapipe_io_lst

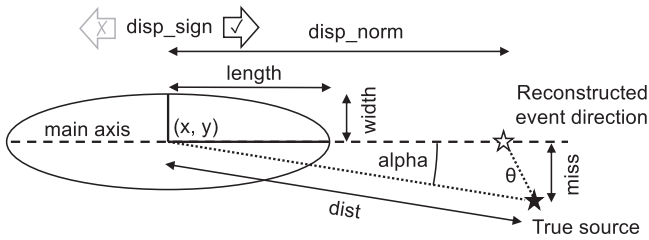


Figure 3. Definition of basic image parameters.

accurately adjusted. In this way they did not deteriorate the optical PSF of the dish. However, the range of the mirror orientation mechanism is not enough to make those mirrors always point outside of the camera limits, which means that they can produce dimmer “duplicate” images of very bright showers in different positions on the camera. By requiring a minimum pixel charge of 3% of the peak charge in the event, we removed all such fake images present in the data. This cut also removes some pixels in the actual tails of (very bright) images, but we verified via MC simulation that this had no negative impact on the performance of the standard event reconstruction described in this paper (including the gamma / hadron separation capabilities).

The cleaned images are then parameterized by a modified version of the Hillas parameters, first described in Hillas (1985), and higher-order moments. The complete list of parameters and their description is presented in the Appendix A.1. These parameters are fed to machine-learning algorithms (random forest; Breiman 2001) for the subsequent steps in the event reconstruction.

3.3. Random Forest Training

Image parameters are used to train random forests using `scikit-learn` (Pedregosa et al. 2011) to reconstruct the desired physics parameters: the direction and energy of the primary, and a *score* (which we call *gammaness*) indicating how likely it is that the primary is a gamma ray, rather than a proton or other cosmic-ray particle. The hyperparameters of the models are presented in the Appendix A.2 for complete reproducibility.

3.3.1. Direction Reconstruction

To reconstruct the incoming direction of shower primaries, we use a version of the *disp* method presented in Lessard et al. (2001). We assume that the point that corresponds to the event direction is located along the main image axis (as expected, within statistical fluctuations, for gamma-ray initiated showers). Two random forests models are trained using gamma MC as input: a regressor for *disp_norm* and a classifier for *disp_sign*, where *disp_norm* is the distance between the image centroid (x, y) and the point along the axis that is closest to the true gamma-ray direction, and *disp_sign* represents on which side of the centroid, along the major axis, the true direction lies (see Figures 3 and 4). The image parameters used as input for the models are *log_intensity*, *width*, *length*, *wl*, *skewness*, *kurtosis*, *time_gradient*, *leakage_intensity_width_2*, *az_tel*, and *alt_tel*.

3.3.2. Energy Reconstruction

For the energy reconstruction, we use a random forest regressor trained to reconstruct the log of the true energy in teraelectronvolts with the following parameters: *log_intensity*,

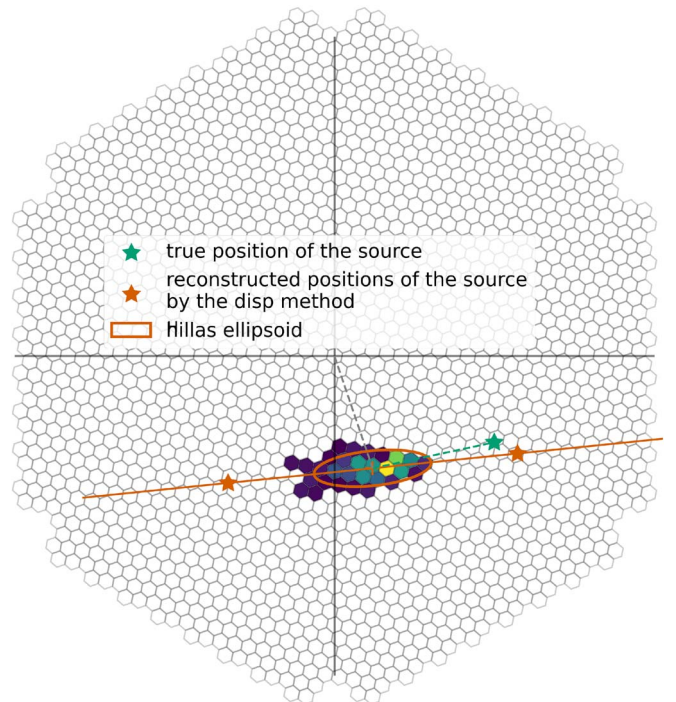


Figure 4. Reconstruction of the source position in the camera frame. The true gamma-ray direction (source position) is shown in green, while in orange are shown the two possible reconstructed source positions determined by *disp_norm* along the major image axis. The final source position will be determined by *disp_sign*.

width, *length*, *x*, *y*, *wl*, *skewness*, *kurtosis*, *time_gradient*, *leakage_intensity_width_2*, *az_tel*, and *alt_tel*.

3.3.3. Particle Classification

For the particle classification, a random forest classifier is trained with the same parameters as the *disp* ones, augmented with the output of the first steps: *log_reco_energy*, *reco_disp_norm*, and *reco_disp_sign*.

The relative importance of the training parameters for each model is reported in Figure 5. It is computed using `scikit-learn` implementation as the mean (and standard deviation for the error bars) of the total reduction of the Gini impurity (Breiman et al. 1984) brought by each feature over all of the trees in the random forest. It is noteworthy that different models preferentially base their decision based on different parameters. We can also recognize the importance of the timing information for a single telescope such as LST-1, in particular to determine the event direction. As a proxy for the impact distance, *time_gradient* is also of major importance for the energy reconstruction with a single IACT (Aliu et al. 2009). Note that Figure 5 shows the relative importance of the parameters for the full MC training sample, considering events of all energies (and it is therefore dominated by events close to the energy threshold).

The models’ hyperparameters (e.g., the number and depth of the trees) have been chosen to achieve good physics performances while keeping the computing footprint manageable, one of the limitations being the memory usage during training. The handling of the models’ training and production of the IRFs has been done on the collaboration computing cluster located on-site at La Palma thanks to the library

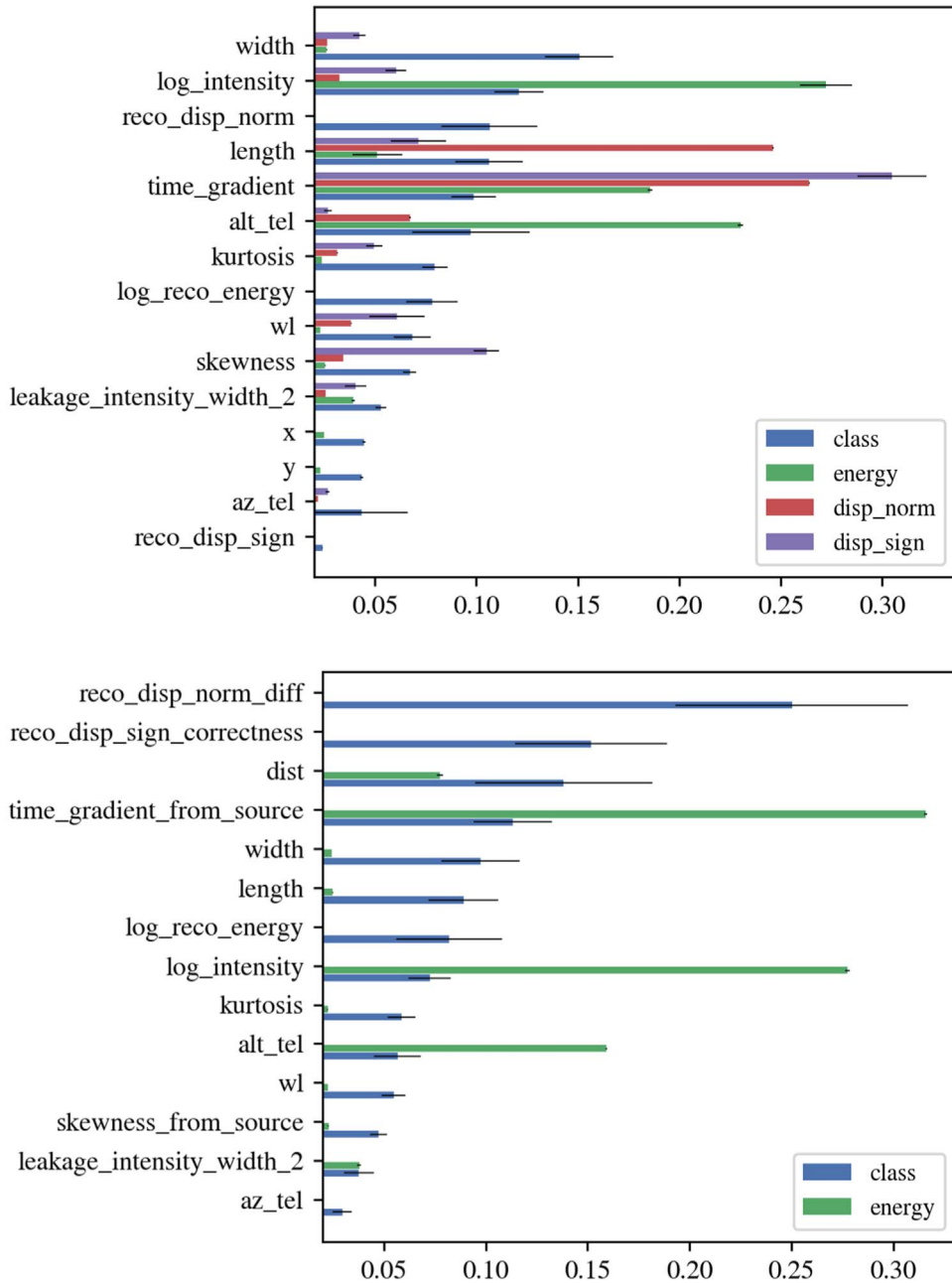


Figure 5. Relative features importance for the different random forests. The top panel is for the source-independent analysis, while the bottom panel is for the source-dependent analysis. Note that there are correlations among the parameters, so the true importance of a given parameter may be slightly different to the one shown here. It can also depend on the energy range: the displayed values are for the whole sample of events surviving image cleaning.

1stMCpipe (Garcia et al. 2022; Vuillaume et al. 2022) developed specifically for that purpose.

3.4. Instrument Response Functions

After training, the random forest models are applied to the MC in each of the test sample pointing nodes (see Figure 1) to compute the IRFs in those directions. The IRFs are used to assess the performances of the LST-1 as a function of the energy and pointing direction, and later used for data analysis.

3.4.1. Effective Collection Area

The effective area is defined as the ratio of reconstructed gamma rays (after event selection cuts) over the number of

simulated ones, multiplied by the area (orthogonal to the incident direction) over which events have been simulated. It is computed as a function of the true energy.

3.4.2. Energy and Angular Resolution

With θ being the angular distance between the true gamma-ray direction and the reconstructed one, the angular resolution θ_{68} is typically defined as the angle within which 68% of the reconstructed θ -values are contained. It is computed as a function of the true energy. The gamma-ray PSF for a single IACT has a central component made of events with properly determined head-tail image orientation (i.e., correctly reconstructed $disp_sign$; see Figures 3 and 4), and, especially at low energies, a separate tail made up by events with wrong

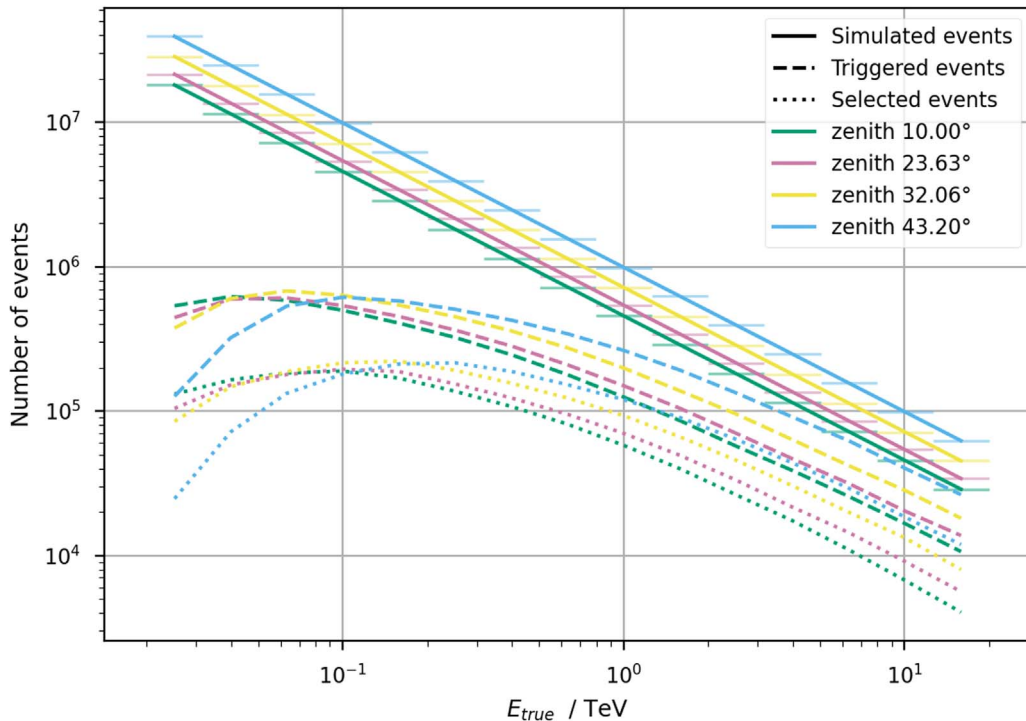


Figure 6. Number of simulated, triggered, and selected events to compute the effective area and other IRFs presented in the right panel of Figure 8 (gamma efficiency = 0.7).

orientation. Near the threshold, the fraction of correctly oriented images is less than 60%, but it increases quickly with energy (see Section 3.6). In order to characterize the central part of the PSF (which is the relevant one to show, e.g., the capability of the instrument to resolve two nearby pointlike sources), we consider only the population of all well-oriented MC gamma rays in the computation of θ_{68} . Note that in the analysis of the observations of extended sources, or of fields with several sources, the complex shape of the PSF at low E should in principle be taken into account. In practice, however, the LST1 performance in those cases is more strongly limited by the modest background rate suppression characteristic of a monoscopic instrument.

The relative energy resolution is defined as the value of the quantity $|E_R - E_T|/E_T = |\Delta E|/E_T$ within which 68% of the reconstructed gamma-ray events are contained, where E_T is the true energy and E_R is the reconstructed energy. The energy bias is computed as the median of $\Delta E/E_T$. Both resolution and bias are computed as a function of the true energy.

The IRFs are computed using the `pyirf` package (Nöthe et al. 2022) after some necessary event selection cuts. A global event selection $intensity > 50$ p.e. is applied (see Section 4), followed by an energy-dependent cut in $gammaness$ (a minimum required value), calculated to keep a given fraction of the MC gamma rays in each bin of reconstructed energy E_R . Finally, for the effective area and energy resolution and bias, we apply an energy-dependent θ cut, which keeps in each bin of E_R 70% of the MC gamma rays with best direction reconstruction (among the well-oriented ones; see above). The numbers of simulated, triggered, and selected events to produce the effective area and the other IRFs are presented in Figure 6 for each zenith angle. It can be seen that the statistics per bin after all cuts, up to 20 TeV, are larger than several thousand events (above 10^4 for most of the energy range); hence, we expect the statistical uncertainties in the IRF computation to be

typically below the percent level. Note that even though we reuse the simulated showers by detecting each one from 10 different telescope locations, after all cuts, the average number of times a shower appears in the final sample is $\simeq 1.0$, 1.4 and 2.0, below 100 GeV, at 1 TeV, and at 20 TeV, respectively.

The resulting IRFs are presented in Figure 7. The left panels provide them for a zenith angle of 10° and for several efficiencies of the $gammaness$ cut. As one can expect, the reconstruction performance generally improves (better resolutions and lower bias) with lower efficiencies (due to stricter event selection), at the expense of collection area. An exception to that rule can be seen in the energy resolution near threshold, possibly because in that range, a tighter gamma-ray selection cut may also entail the selection within an E_T bin of up-fluctuations in terms of, e.g., Cherenkov light yield, leading to a larger energy reconstruction bias.

The best performances at low zenith (10°) are achieved in the teraelectronvolt range, with an angular resolution between $0^\circ.1$ and $0^\circ.2$ depending on the gamma-ray selection efficiency, a relative energy resolution down to 15%, and a bias of 5%. Below 100 GeV, performances decrease rapidly but stay relatively constrained at low zenith. The right panels of Figure 7 present IRFs for a fixed gamma-ray selection efficiency of 70% and for zenith angles between 10° and $43^\circ.2$, close to the zenith angles of the observations presented in the next section. We currently have no explanation for the “bump” in the energy resolution curves (located around 70 GeV for low zenith), but it seems a genuine feature: it has a smooth structure when finer E-binning is used, and it appears, slightly shifted in energy, at different zenith angles.

3.5. Source-dependent Analysis

The event reconstruction performance using a single telescope image is expected to be worse than the stereoscopic

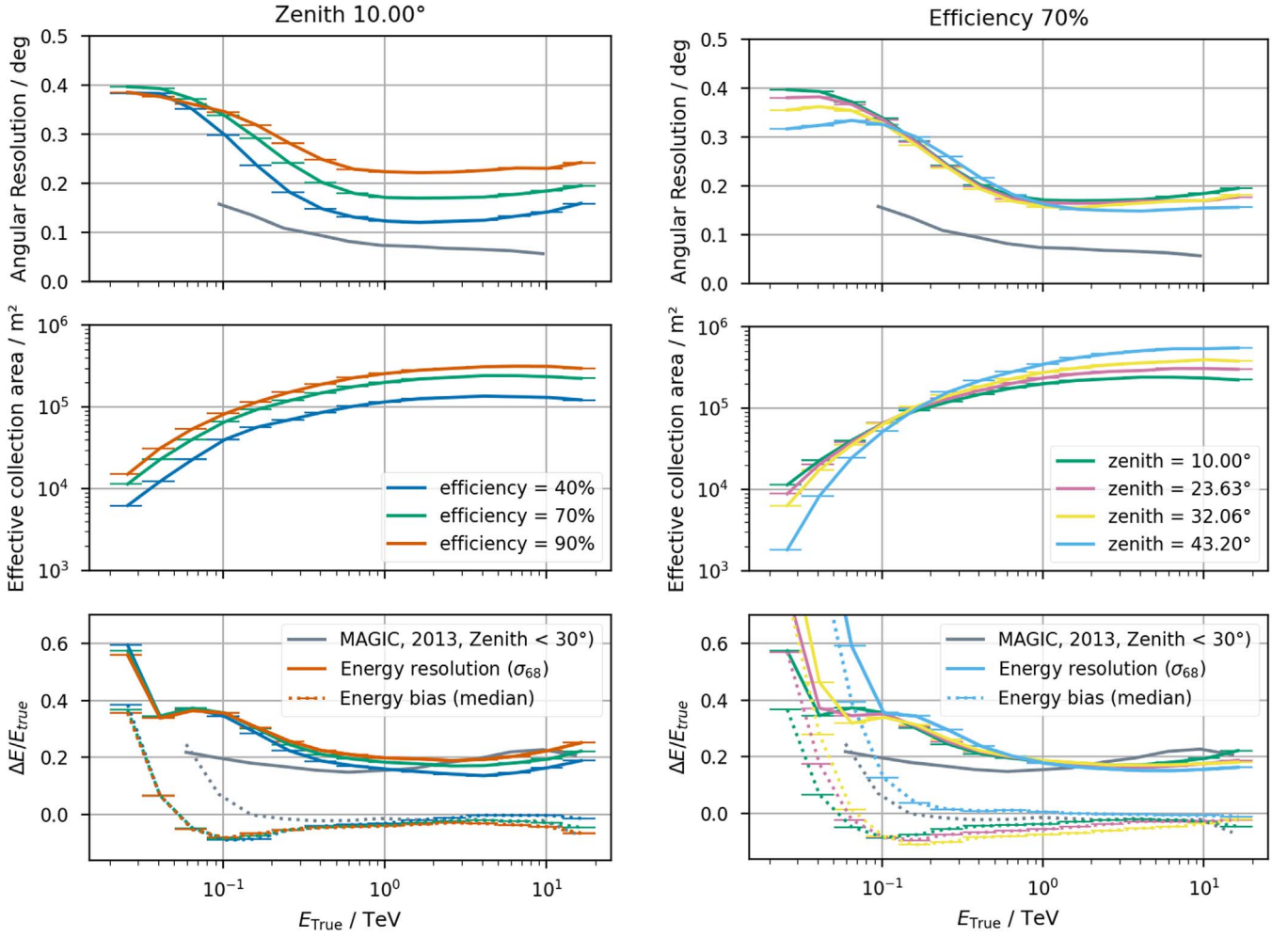


Figure 7. IRFs as a function of the true energy. Left panels: fixed zenith = 10° and several gamma-ray efficiencies; right panels: fixed gamma-ray efficiency = 70% for several zenith angles. Top panels: the angular resolution; middle panels: the effective area; bottom panels: the energy resolution and bias. Angular and energy resolution are best at intermediate energies, worsening toward high energies due to the truncation of the large-impact shower images, and toward low energies due to the less precise reconstruction of small and dim showers. The performances of MAGIC extracted from Aleksić et al. (2016) are shown for comparison.

reconstruction, especially in the low-energy range. To improve the monoscopic analysis performance, an a priori assumption of the gamma-ray source position may be advantageous. In the case of a single pointlike gamma-ray source in the telescope field of view, all gamma rays are expected to arrive from the same direction. A powerful parameter used in the source-dependent analysis is *dist* (see Figure 3), which is the distance between the known source position and the centroid of the shower images. Since *dist* correlates with the shower impact parameter inside the light pool (Aliu et al. 2009), it improves the energy reconstruction performance.

For source-dependent analysis, the signs of *skewness* and *time_gradient* are redefined based on the known source position, and the parameters are renamed *skewness_from_source*, *time_gradient_from_source*. Those source-dependent parameters including *dist* are used as input parameters of the random forest training. For proton MC, we use a single fixed point 0.4° away from the camera center to compute the source-dependent parameters. Thus, the image centroid coordinates (x , y) are removed as training input parameters for source-dependent analysis to avoid bias.

For the particle classification, two extra parameters (*reco_disp_norm_diff* and *reco_disp_sign_correctness*) are introduced based on the comparison between the direction

reconstruction and the known source position. The former is the absolute value of the difference between *reco_disp_norm* and *dist*, and the latter is the estimated probability (see the Appendix A.1) that the known source position is the correct one for the given image. Both are measures of how consistent the result of the *disp* method is with the known position of the source. The input parameters used for the source-dependent analysis are also shown in the bottom panel of Figure 5. It can be seen that the four most relevant parameters for image classification use the knowledge of the source position.

In addition to including the additional parameters, in the random forest training we only use gamma-ray simulation events with incident direction within 1° of the telescope pointing (a compromise between keeping good training statistics while excluding events with significantly larger off-axis angles than the Crab has in the real observations).

To compute the excess counts, the *alpha* angle (the angle between shower axis and the line between the known source position and the image centroid, see Figure 3) is used instead of θ for the source-dependent analysis. The IRFs for source-dependent analysis are presented in Figure 8, again for several gamma-ray efficiencies and zenith angles. In this case, the angular resolution cannot be computed because the direction of gamma-ray events is assumed to be known. The

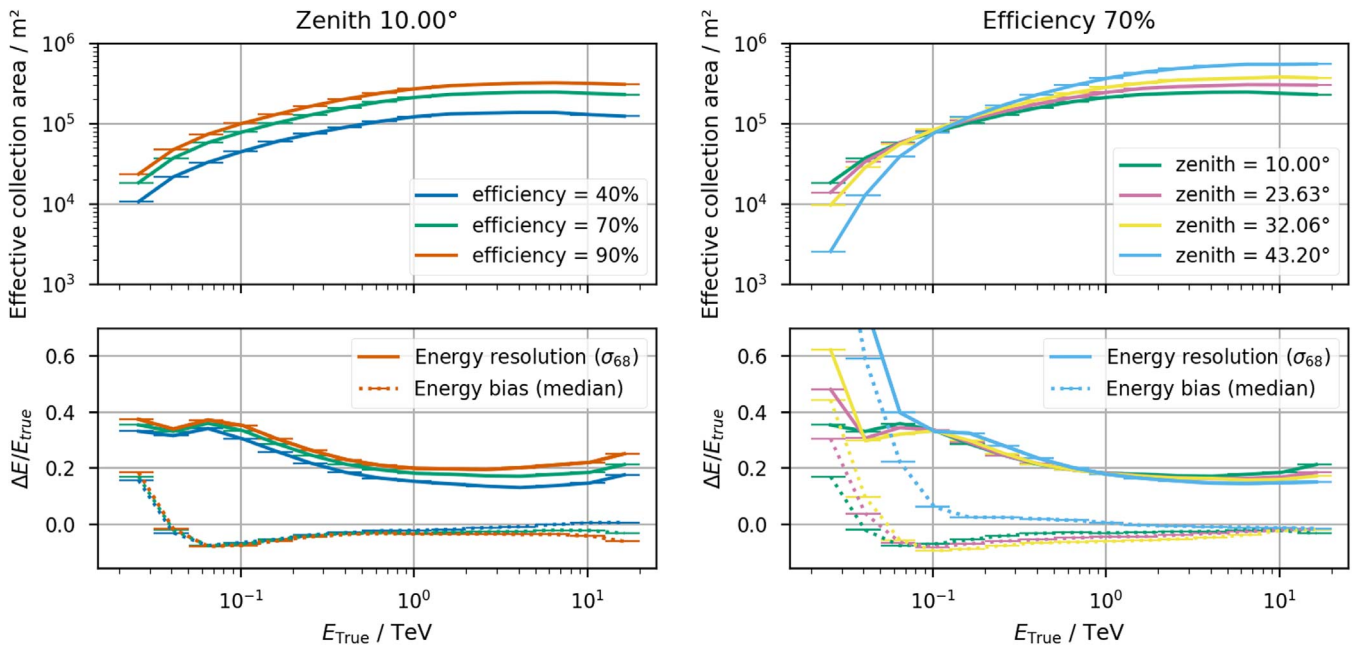


Figure 8. Evolution of the source-dependent analysis IRFs as a function of the true energy. Left panel: fixed zenith = 10° and several gamma-ray efficiencies. Right panel: fixed gamma-ray efficiency = 70% and several zenith angles. Top panels: the effective area. Bottom panels: the energy resolution and bias. The energy resolution shows the same general trend as for the source-independent analysis, but with a significantly better value in the first bin.

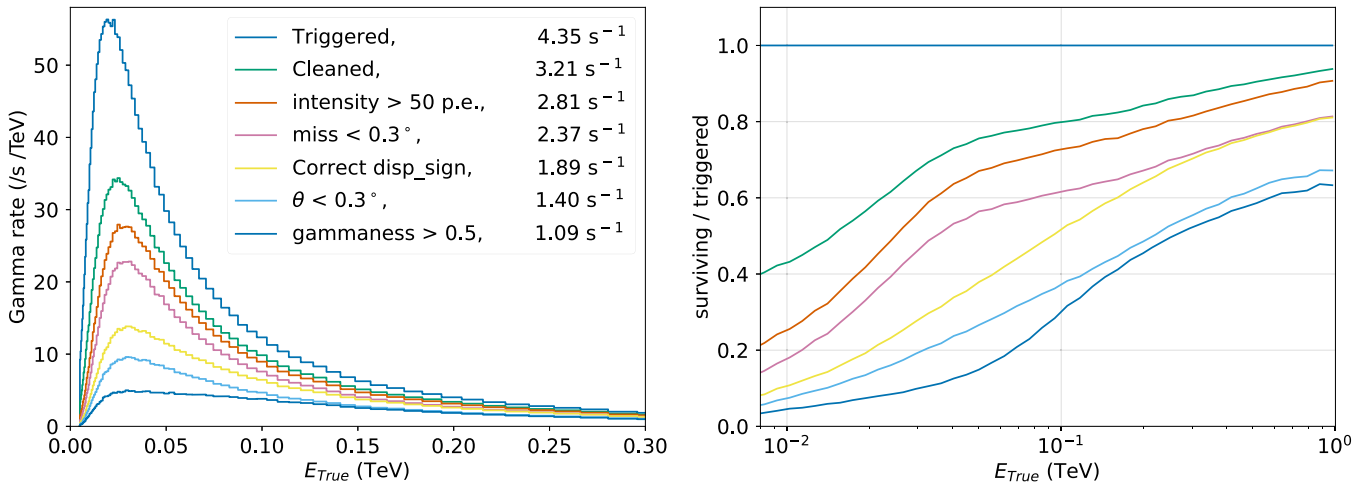


Figure 9. Left: distribution of the true energy of MC gamma-rays observed at 10° zenith angle, at different stages of the standard source-independent analysis. Energy-dependent weights are applied to the events to reproduce a Crab-like spectrum (from Aleksić et al. 2015), resulting in the quoted event rates. The peak energy for triggered events (often used as a definition of energy threshold) is at ≈ 20 GeV. The peak shifts to ≈ 25 GeV after cleaning, and ≈ 30 GeV when we require a minimum image *intensity* and exclude events with bad reconstruction of the image axis (“miss” is the distance between the true gamma-ray direction on the camera and the reconstructed axis; see Figure 3). Right: fraction of triggered events that survive the different stages of the analysis, plotted vs. energy. Below 100 GeV, due to the limitations of monoscopic shower reconstruction, a majority of the surviving gamma-ray events have poorly reconstructed direction and/or are hard to distinguish from the background.

applied selection cuts for the IRFs are then: *intensity* > 50 p.e., the gamma-ray efficiency, and an additional α -cut-efficiency = 70% (similar to the θ -efficiency) for the effective area, energy resolution, and energy bias. The obtained IRFs are very similar to those of the source-independent analysis, the main difference being a visible improvement of the energy reconstruction in the first two energy bins (i.e., true energy below 50 GeV). There is also an increased effective area at low energies (by around 40% under 50 GeV)—due to events that in the source-independent analysis are reconstructed far away from the source because of wrong head-tail assignment.

3.6. Energy Distribution of Gamma Rays in Different Analysis Stages

The energy threshold of an IACT is often defined as the energy at which the distribution of the true energies of the detected events peaks, for a given assumed spectrum (usually that of the Crab Nebula). Figure 9 shows the E_{True} distributions for low-zenith (10°) MC gamma rays at trigger level and at different stages of the analysis. The simulations are tuned to the current trigger configuration of the telescope (see Section 4). The trigger threshold is about 20 GeV, which rises to ≈ 30 GeV after selecting the events that survive the cleaning stage, have an image *intensity* of at least 50 p.e., and have a well-

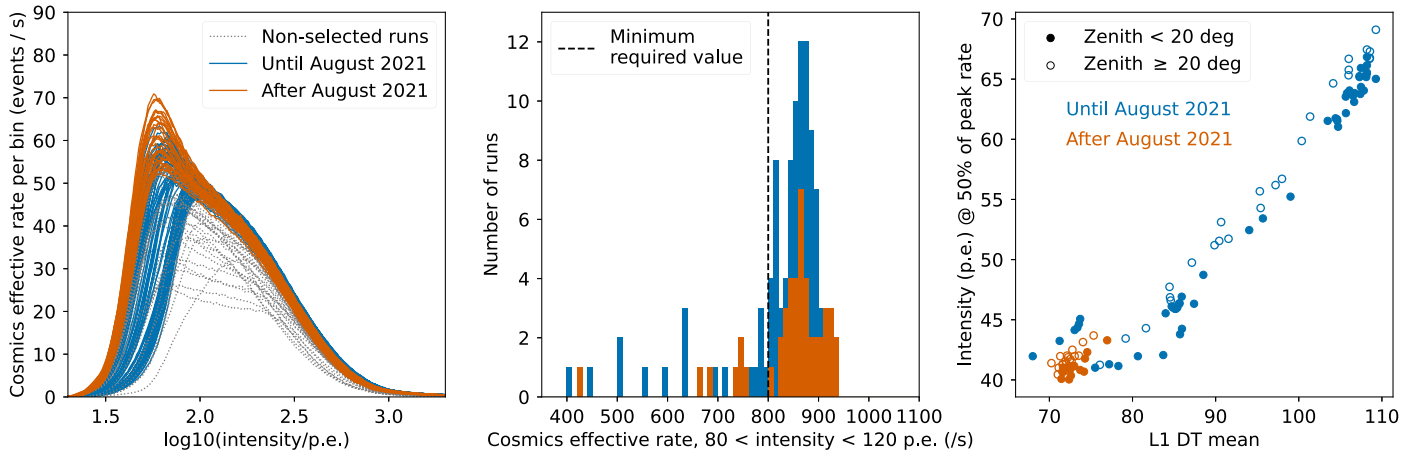


Figure 10. Left: run-wise image *intensity* distributions (for shower events). Each curve corresponds to a data run. The large differences seen below 80 p.e. among the selected runs are related to the different trigger settings of the telescope, which did not become stable until 2021 August. The differences in the peak rates among the post-2021 August data are mostly connected to the different ZDs, which span the range 6° – 35° . Center: rate of cosmics in the *intensity* range between 80 and 120 p.e. The runs with a value below 800 s^{-1} are discarded. Right: correlation between the position of the rising edge of the *intensity* distributions and the camera-averaged trigger threshold setting. The deviation from the linear behavior at low thresholds is related to the image cleaning, which removes the faintest among the triggered events.

reconstructed image axis (closer than 0.3° to the true direction). Naturally, the loss of events in all of the analysis steps is larger near threshold than it is at higher energies. Below 100 GeV, nearly half of the events for which a reasonably *well-oriented* image main axis has been reconstructed get a poor direction reconstruction because of wrong head-tail assignment (*disp_sign*), or poor *disp_norm* reconstruction. This just means that for faint, few-pixel images, determining the plane that contains the shower axis and the telescope location (except at very low impact parameter) is much easier than determining the direction of the axis within that plane. That is the main reason why stereoscopic reconstruction enormously improves the performance of IACTs: additional images of the same shower provide more such planes, from whose intersection a full 3D geometrical reconstruction of the shower axis can be achieved. It is also the reason why source-dependent analysis results in improved energy resolution for a single IACT.

Figure 9 also illustrates the fact that, for a fixed *gammaness* cut, the loss of gamma-ray events is always larger at lower energies, i.e., the background discrimination power in monoscopic analysis decreases quickly as the images become fainter. As we will see, the lack of stereoscopic reconstruction means that despite its large mirror area and lower-energy threshold, LST-1 operating in monoscopic mode cannot outperform (in the overlapping energy range) the existing arrays of IACTs with significantly smaller mirror dishes.

4. The Data Sample

The data used in this study were recorded between 2020 November and 2022 March. We have focused on the analysis of low-zenith Crab observations performed in wobble mode (Fomin et al. 1994), which facilitates the task of estimating the rate of background events recorded together with the signal. The telescope was pointed 0.4° away from the center of the Crab Nebula, alternating between two different sky directions on opposite sides of the source. Each observation run with a given sky pointing lasted typically for 20 minutes. A total of 57.2 hr of observation with the telescope pointing within 35° of the zenith were collected. Of those, 48.0 hr correspond to dark-night observations, i.e., with the Moon below the horizon. This

is our starting sample. The zenith and dark-night constraints are aimed at achieving a low gamma-ray energy threshold of around 20 GeV. The next step was to identify the data taken under good atmospheric conditions. The total shower trigger rates are affected by weather conditions (which modify the atmospheric transmission), but also by variations in the telescope trigger settings. During this period, the telescope was in its commissioning phase, and different trigger settings were tested (including different algorithms for the dynamic modification of the settings during observations, to react to the presence of stars in the field of view). This means that the threshold of LST-1 was not stable (see right panel of Figure 10), and hence the *total* shower trigger rates are not a good proxy of the quality of the atmospheric conditions during this period. Instead of total rates, we used two quantities that are not affected by the trigger settings, because they are determined by showers well above the threshold: the camera-averaged rate of pixel pulses with charge above 30 p.e. (*pix_rate* $q_{>30}$), and the rate of shower images with *intensity* between 80 and 120 p.e. (R_{80-120}) (see the central panel of Figure 10). We calculated the run-averaged values for those quantities, and removed from our sample runs with *pix_rate* $q_{>30} < 4.5 \text{ s}^{-1}$ or $R_{80-120} < 800 \text{ s}^{-1}$. The cuts are just intended to remove outliers, and the specific cut values are to a certain extent arbitrary. The total observation time of the 117 surviving runs amounts to 35.9 hr. Using the distribution of time intervals between consecutive triggered events, we estimated the dead time to be around 4.7%, resulting in an effective observation time (live time) of 34.2 hr.

The left panel of Figure 10 shows the run-averaged distributions of shower image intensities. The gray dotted lines correspond to runs that were rejected by the cut in R_{80-120} . The rest of the distributions are those of the selected runs. Above ≈ 80 p.e., all of the spectra agree pretty well, with the maximum and the minimum rates differing by less than 20% (with part of this spread being actually due to the different zenith angles). Below 80 p.e., in contrast, large differences appear, caused by the variations in the trigger settings discussed above. We can characterize the threshold of each of these distributions by the value of $\log_{10}(\text{intensity}/\text{p.e.})$ at which 50% of the peak event rate is reached. The right panel of

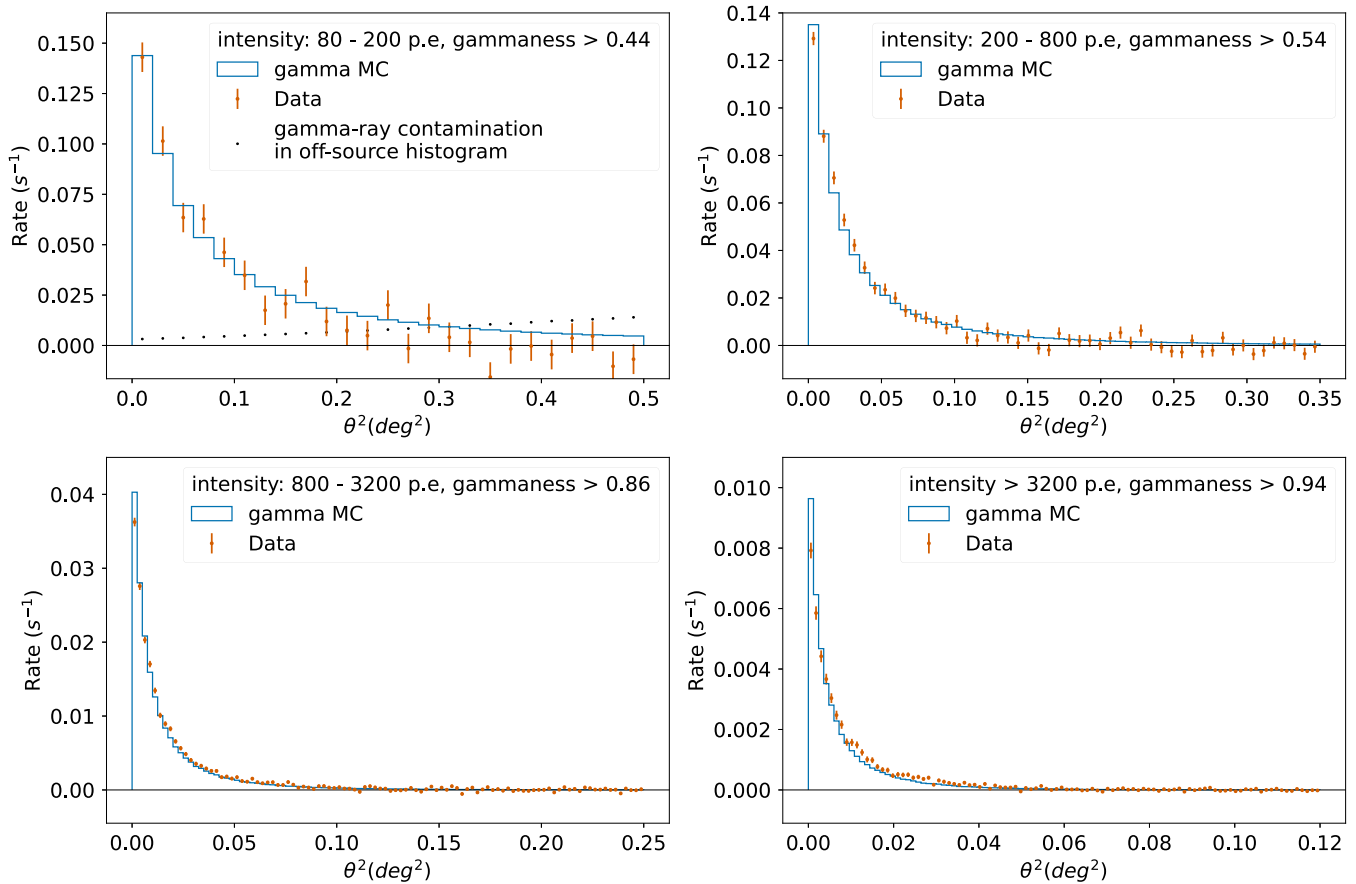


Figure 11. Comparison of θ^2 distributions, gamma MC simulations vs. Crab Nebula excess events. The observed discrepancies may be partly due to arcminute-scale mispointing of the telescope.

Figure 10 displays that parameter (converted to p.e.) as a function of the camera-averaged trigger threshold setting during the run: the plot clearly shows that the differences among the *intensity* distributions are indeed mostly due to the different trigger settings. The current configuration of the trigger settings was established in 2021 August. The data taken since then (see orange curves in Figure 10, left) are much more stable and have a lower threshold.

The trigger threshold in the MC simulations has been set to the lowest value found in the data, i.e., it is tuned to the post-2021 August situation. This means that in order to achieve a good match between the full data sample and the simulations, we have to apply a “software trigger” to equalize data and MC. In this analysis we apply a simple cut in image *intensity*. A cut *intensity* > 80 p.e. brings all of the data to a common “analysis threshold” and ensures a good match of MC and data. For data taken after 2021 August, a cut *intensity* > 50 p.e. is enough to achieve the same goal.

5. Validation of the MC Simulation through Comparisons with Data

We have used the observations of the Crab Nebula to validate the MC simulation of the detection of gamma-rays with LST-1. We do this through comparison of the distributions of image parameters for the simulated gamma-ray images, and those obtained for the gamma-ray excess recorded from the direction of the Nebula. For a meaningful comparison, the distribution of the energies of the simulated and observed

gamma rays must be as close as possible. The MC histograms have been filled with event-wise energy-dependent weights calculated to reproduce the log-parabola parameterization of Crab Nebula spectrum reported in Aleksić et al. (2015). For better comparison of the distribution shapes, the overall normalization of the MC histograms is a free parameter, tuned to achieve the best match between the distributions (via a χ^2 -test). The small extension of the Crab Nebula (H.E.S.S. Collaboration 2020) is also simulated using a Gaussian smearing ($\sigma_{2D} = 52''$) of the reconstructed directions in the MC sample. The comparisons are presented in four ranges of image *intensity*, starting at 80 p.e.: 80–200, 200–800, 800–3200, and >3200 p.e. The distributions of true (MC) energy peak, respectively, at $\simeq 30$, 80, 200, and 700 GeV (see the right panel of Figure 13).

We start by comparing the angular distribution of the events around the center of the Nebula. Figure 11 shows the distribution of the θ^2 parameter, the squared angular distance between the reconstructed event directions and the source. The distribution for the gamma rays in the real data is obtained by subtracting the distribution calculated with respect to a control “off-source” direction from the “on-source” distribution in which θ is computed relative to the Crab. The off-source direction is $0^\circ 8$ away from the source direction, with the center of the field of view located exactly between them. The acceptance for background events (mostly proton-initiated showers) is the same around both directions at better than the 1% level, and therefore the subtraction of the two distributions yields the distribution of θ^2 for the gamma-ray excess. The

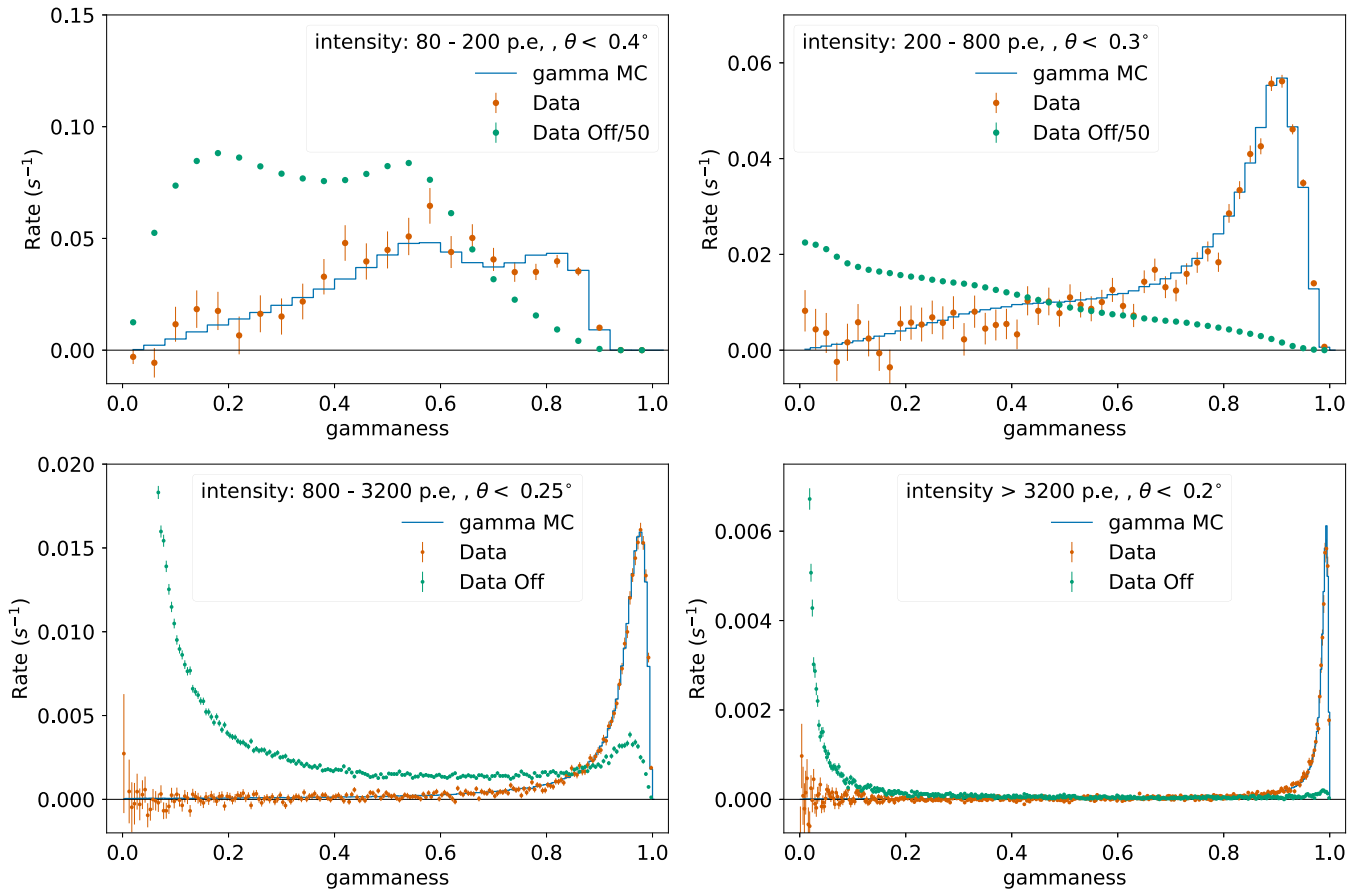


Figure 12. Comparison of *gammaness* distributions, gamma MC simulations vs. Crab Nebula excess events. The improvement of the background discrimination power with the *intensity* of the images is clearly seen. Note that in the top panels the background rates are scaled by a factor 1/50 for better visibility.

distributions are obtained with the events that survive a gamma-ray selection (via a *gammaness* cut), which keeps in each *intensity* range $\simeq 80\%$ of the gamma-ray rate. The cut reduces the background rate, and hence the fluctuations in the subtracted histograms.

In the lowest *intensity* range (80–200 p.e.), the tail of the gamma-ray distribution extends beyond the center of the field of view, and a small correction is necessary to account for the expected gamma-ray contamination in the bins of the off-source histogram. The correction is shown by the black dots on the top-left panel of Figure 11. As expected, the quality of the direction reconstruction improves significantly as we select brighter images. The test also shows that the MC distributions are generally narrower than those of real data. The difference becomes more noticeable as *intensity* increases and angular resolution improves. This hints at the possibility that the difference between data and MC is mostly due to arcminute-scale variable mispointing (note that no offline pointing corrections have been applied in this analysis). We tested this hypothesis by introducing in the MC simulation a Gaussian smearing of the reconstructed directions. Excellent agreement of the θ^2 distributions on all four ranges of intensity was achieved for a smearing with standard deviation $\sigma = 1/5$ in each axis. This possible mispointing is much smaller than the angular resolution achieved even for the brightest images, and hence poses no major challenge for the higher-level analysis. We expect most of this discrepancy to disappear once we

implement offline pointing corrections based on the observation of stars in the field of view.

For other parameter comparisons, it is important to avoid the bias in the distributions that might be caused by the application of analysis cuts, e.g., the *gammaness* cut described above. The distribution of any image parameter that is used as an input in the random forest that computes *gammaness* would be biased (toward looking more MC-gamma-like) if a cut in *gammaness* was applied to select the events used in the procedure. Obviously, if the parameter is *gammaness* itself, such a cut would simply clip the distribution. For the following parameter comparisons, we therefore use *all* events with reconstructed direction within a given angular distance of the source to produce the distribution of the desired parameter (“on-source”). The angular cuts for the four *intensity* bins ($\theta < 0^\circ.4$, $0^\circ.3$, $0^\circ.25$, and $0^\circ.2$) integrate over 90% of the observed excess. Due to the lack of background rejection, the on-source histograms will contain many more background events than gamma-ray events from the source. We then obtain the corresponding distribution for background-only events, using those recorded around the off-source direction, with the same angular cuts. Like in the case of θ^2 , the subtraction of the off-source distribution from the on-source one yields the distribution of the given parameter for the gamma-ray excess events. The result of this procedure applied to the *gammaness* parameter is shown in Figure 12. The data and MC distributions agree well in all four *intensity* bins. The distribution of *gammaness* for the background events

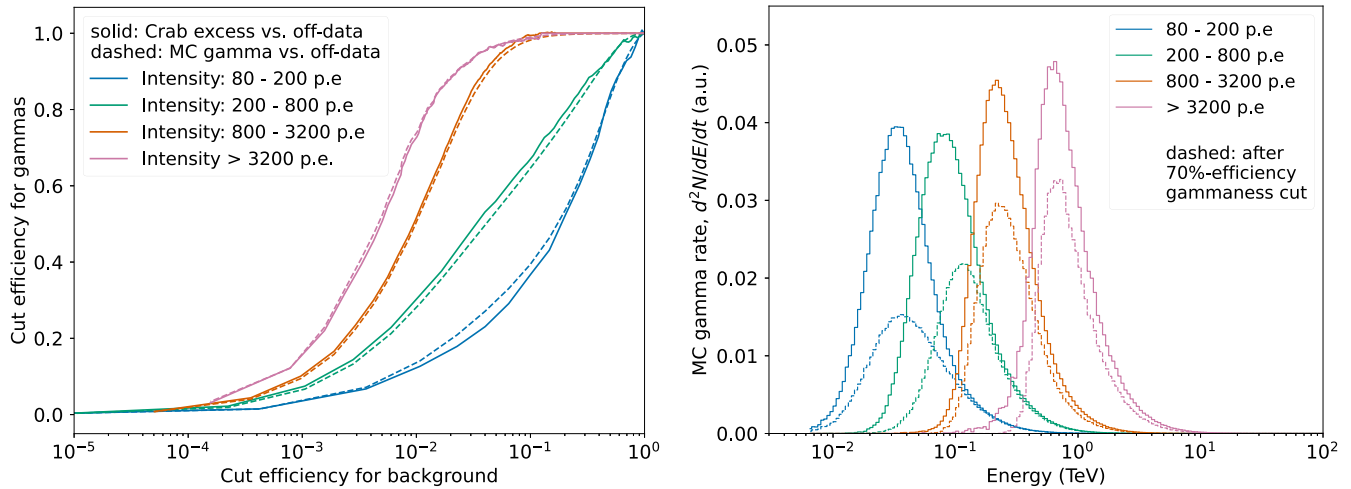


Figure 13. Left: ROC curves of the signal selection cuts. Right: energy distributions of gamma rays in different ranges of image *intensity*. The θ cuts are the same as in Figure 12. Note that the 70% cut efficiency is computed relative to the total gamma rate in each *intensity* bin (which is not proportional to the areas under the curves in this representation with logarithmic energy axis).

is also plotted, clearly showing the increasing background discrimination power of the *gammaness* parameter as image *intensity* gets larger. This can be better seen in the receiver operating characteristic (ROC) curves shown in the left panel of Figure 13. The curves are produced using real off data as background, and the observed Crab excess (solid lines), or the MC gamma rays (dashed lines), as signal. This shows once more that MC simulations reproduce well the actual behavior of LST-1.

The good data–MC agreement of the *gammaness* distributions indicates that the distributions of the individual image parameters (and the correlations among them) that are used in the computation of *gammaness* are also well reproduced by the simulation. We illustrate this in Figure 14, which shows the distribution of four important image parameters obtained in the *intensity* range 800–3200 p.e. (in which the distributions of individual parameters for gamma rays and background already differ significantly).

6. Results

In this section we present the results obtained from the higher-level analysis of the LST-1 observations of the Crab Nebula and pulsar. These include the spectral energy distribution (SED) and light curve of the Nebula, a phaseogram showing the detection of the pulsar, and an estimate of the LST-1 flux sensitivity for pointlike sources.

6.1. Flux Sensitivity

To calculate the sensitivity of LST-1, we follow the definition of detection sensitivity as the minimum flux from a pointlike source that the telescope is able to detect with a 5σ statistical significance in 50 hr, calculated in five logarithmic energy bins per decade and using an ON/OFF ratio of 0.2. Additionally, we require at least 10 detected gamma-rays per energy bin, and a signal-to-background ratio of at least 5%.

The calculation presented here is based on the Crab observations, and hence the result corresponds to the average LST-1 performance at low zenith angles ($<35^\circ$). We divided the Crab data sample into two subsets of the same size (even- and odd-numbered events), which are completely equivalent in terms of telescope pointings and all other observation

conditions. One of the subsets was used to optimize the gamma-ray selection cuts, by scanning a grid of α/θ and *gammaness* cuts, and selecting the cut combination that results in the best sensitivity for each of the energy bins. The optimal cuts were then applied to the other (statistically independent) subset, on which the minimum flux that fulfills all conditions in the definition was computed. This procedure ensures that the sensitivity values are not biased by statistical fluctuations. In the cut scan, only cut combinations that produced at least a 3σ excess from the Crab direction in both subsets are considered.

The result, for source-dependent and source-independent analysis, is shown in Figure 15. The fluxes are given in a fraction of the Crab Nebula flux (“Crab units,” C.U.). The shaded bands show the total uncertainty of the calculation, assuming a $\pm 1\%$ systematic uncertainty in the background normalization: the band edges are obtained by modifying the gamma-ray excess in each bin by $\pm(\sigma_{\text{stat}} + 0.01 N_{\text{off}})$ where N_{off} is the number of events after cuts in the off-source region.

We also calculated the sensitivity using only the condition of 5σ statistical significance in 50 hr (re-optimizing the cuts), to show in which energy range (near threshold) the sensitivity is limited by the systematic uncertainty in background normalization. Note that in observations of, e.g., pulsars in which the background can be estimated from the on-source events recorded in the off-pulse phase range (see Section 6.3), we expect negligible background systematics, and hence gamma-ray excesses of well below 5% of the background can be robustly detected.

The best integral sensitivity (for a Crab-like spectrum) in 50 hr is obtained for $E > 250$ GeV, and is 1.1% C.U. We also computed the integral sensitivity for a 0.5 hr exposure, given the fact that short-time observations of transient events are one of the main goals of LSTs, and we reach an integral sensitivity of 12.4% C.U. above 250 GeV.

Somewhat surprisingly, the performances of the source-independent and source-dependent analyses in terms of flux sensitivity are very similar, with the latter only slightly better at the highest energies. It seems that, with the current analysis, the introduction of the a priori known direction of the pointlike source in the event reconstruction does not significantly improve the background suppression capabilities.

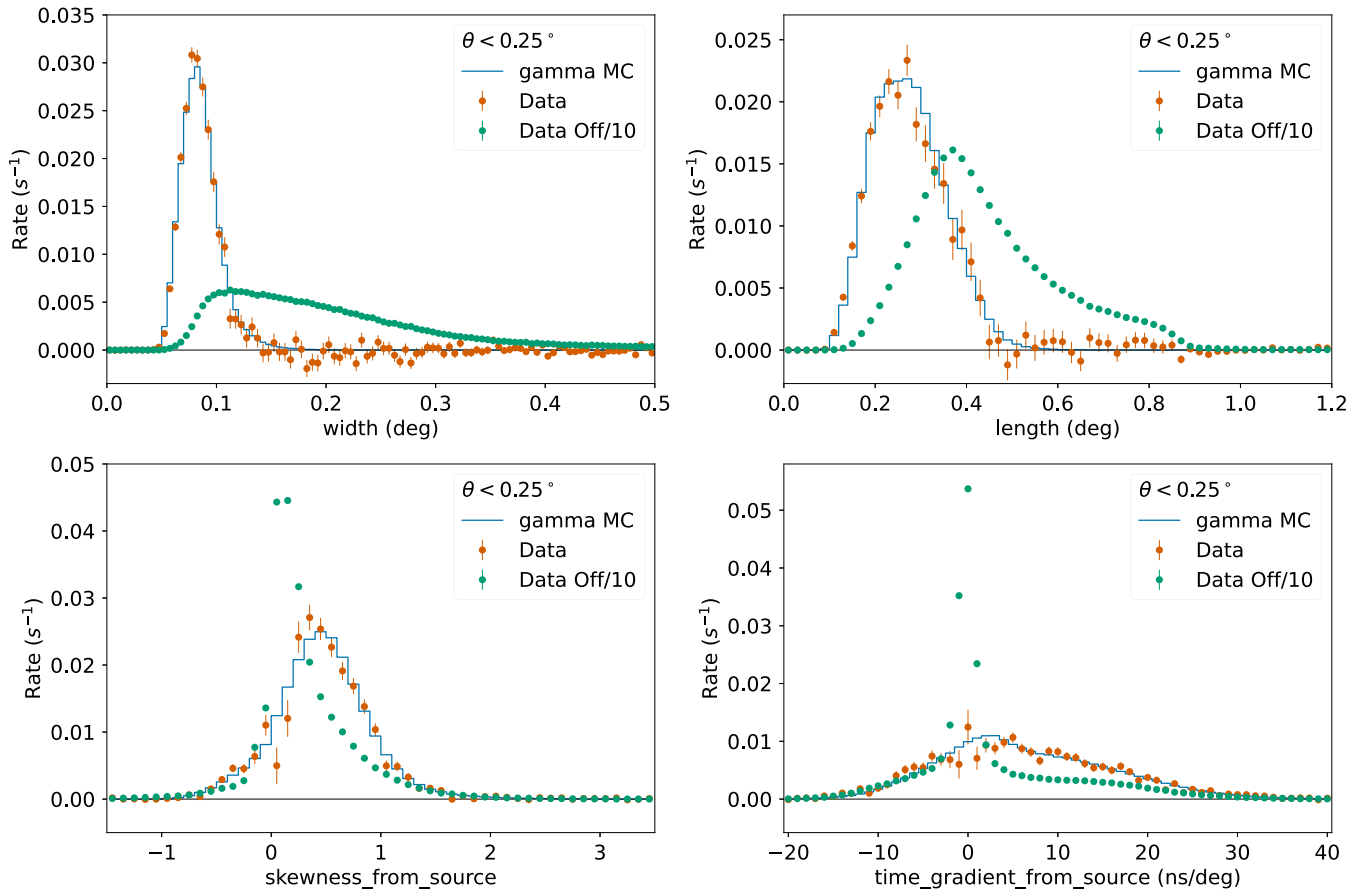


Figure 14. Distribution of several image parameters for events in the *intensity* range 800–3200 p.e., gamma MC simulations vs. Crab Nebula excess events. The sharp peak at 0 in the time gradient distribution of the background (bottom-right panel) is mostly due to events dominated by single muons. In the bottom plots, the sign of the skewness and time gradient parameters is defined relative to the true source position, to show the asymmetry that allows us to determine the head-tail orientation of the shower images.

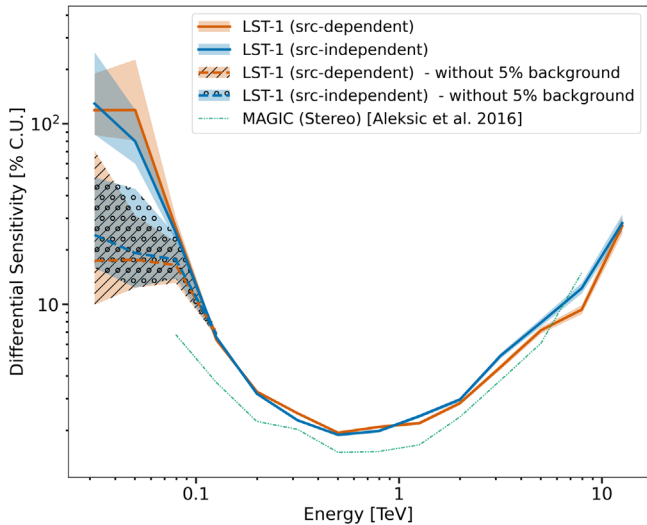


Figure 15. Differential sensitivity for source-dependent and source-independent analyses, vs. reconstructed energy, with and without including the condition that the signal-to-background ratio has to be at least 5%. The MAGIC reference is taken from Aleksić et al. (2016).

The MAGIC sensitivity (Aleksić et al. 2016) is also shown for comparison in Figure 15: as expected, despite the larger mirror area of LST-1 compared to that of the MAGIC telescopes, the advantages of stereoscopic reconstruction can

be clearly seen in the plot. Above 100 GeV, MAGIC has a factor ~ 1.5 better sensitivity on average. At lower energies, the difference actually increases, despite the lower LST-1 threshold. The smallest difference is seen at the highest energies, a result of the much larger field of view of LST-1, which provides larger reach in impact parameter.

6.2. Crab Nebula Spectrum and Light Curve

Aside from the metrics presented in previous sections, we assess the performance of the telescope by extracting the SED and light curve of the gamma-ray emission from the Crab Nebula, known to be stable in the VHE band, and comparing them with previous measurements reported by other instruments. DL3 data, containing gamma-like event candidates and the IRFs, are further processed using Gammapy v0.20 (Donath et al. 2022) to produce these high-level results for the two analysis approaches mentioned above. The LST-1 SEDs also include a small contribution from the pulsar at the lowest energies (estimated from Ansoldi et al. 2016 to be $\simeq 10\%$ and 2% of the total flux at 30 and 100 GeV, respectively), which is smaller than the total uncertainty and has *not* been subtracted in this analysis.

The event selection starts with an image *intensity* cut of >80 p.e. for the analysis of the entire data set (relaxed to >50 p.e. for the separate analysis of the post-2021 August subset), as explained in Section 4. The gamma-ray candidates are then chosen by applying energy-dependent *gammanness* and angular

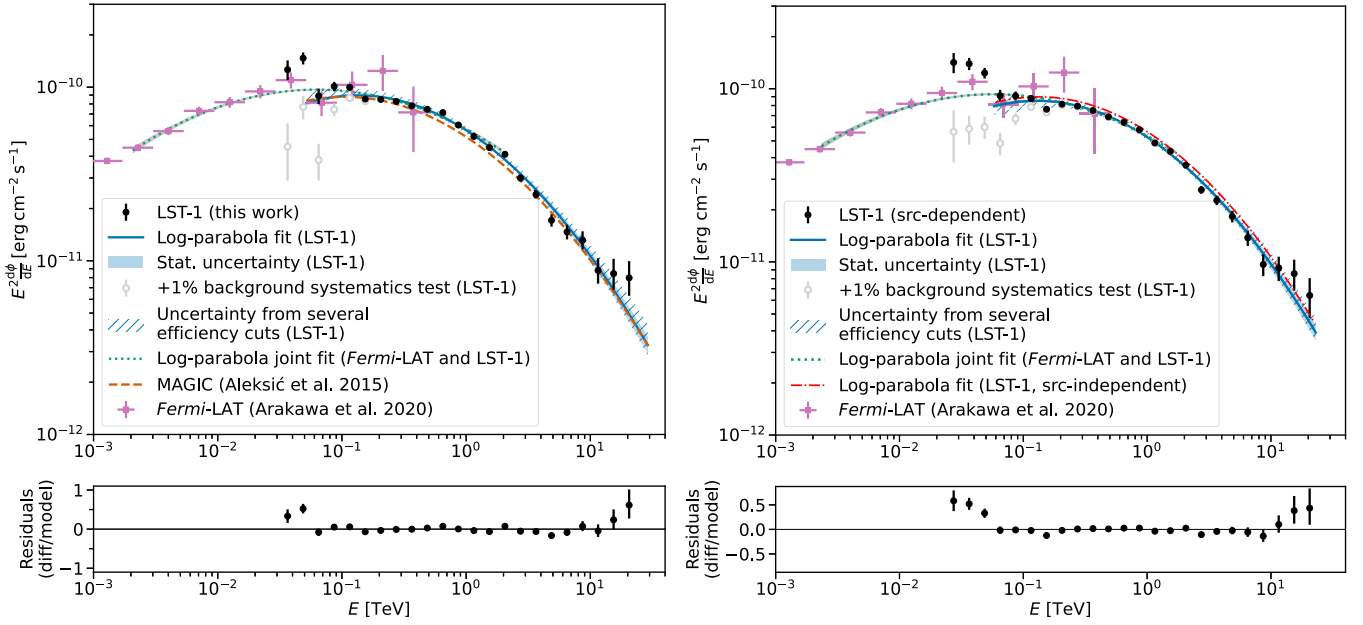


Figure 16. SED of the Crab Nebula for the entire LST-1 data set obtained with the source-independent analysis (left panel) and source-dependent analysis (right panel). Flux points (black circles) and best-fit model (solid blue line) correspond to the data set with a cut in image *intensity* > 80 p.e., and energy-dependent *gammaness* and θ/α (source-independent/source-dependent) selection cuts with 70% gamma-ray efficiency. The solid error band illustrates the statistical uncertainty of the fit. Open markers represent the effect of increasing the background normalization by 1%, to show that even such a small systematic error can have a large effect, well beyond the statistical uncertainty, on the flux at the lowest energies. The joint fit of the Fermi-LAT and LST-1 spectra is represented by the dotted line (accompanied by its statistical uncertainty band). The SED model obtained with the source-independent analysis is also shown for comparison in the right panel (red dotted–dashed line).

cuts that keep a given percentage of the MC gamma-ray events in each bin of reconstructed energy. As baseline settings, we decided to use 70% efficiency for both the *gammaness* and the θ cuts. Additionally, we set maximum values 0.95 for the *gammaness* cut and $0^\circ.32$ for the θ cut.

Since the data set fully consists of observations performed in wobble mode, we can estimate the residual background in the signal region by using the event count in a control off-source sky region within the field of view, as explained in Section 5.

We then perform a forward-folding likelihood fit in the energy range 50 GeV–30 TeV for straightforward comparison with the MAGIC reference (Aleksić et al. 2015) assuming a log-parabola spectral shape for the differential energy spectrum:

$$d\phi dE = f_0 \cdot (E/E_0)^{-\alpha - \beta \log(E/E_0)} [\text{cm}^{-2} \text{s}^{-1} \text{TeV}^{-1}], \quad (1)$$

where $E_0 = 400$ GeV was chosen close to the decorrelation energy (energy at which the normalization of the spectrum, f_0 , is least correlated with the other spectral parameters), and \log is the natural logarithm. The best-fit model for the entire data set is shown in the left panel of Figure 16, and the resulting spectral parameters are listed in Table 1. Additionally, using the Gammapy utility `FluxPointsEstimator`, we display the flux points calculated based on this spectral model considering eight bins per decade logarithmically spaced. The procedure followed to obtain the flux normalization in each energy bin is described in Acero et al. (2015). Since the fitting range of the model starts at 50 GeV, lower-energy flux points up to 1 TeV are instead computed taking into account the joint model fit of the Fermi-LAT and LST-1 data sets (see description below).

In order to check that the SED model does not significantly change with the applied gamma-ray efficiencies, we obtained

the SED for different combinations of *gammaness* and θ selection cuts, with (40, 70, 90)% gamma-efficiency for *gammaness* and (70, 90)% in the case of θ . Tighter θ cuts are not advisable, given the discrepancies shown in Figure 11. The envelope of the resulting SEDs is shown as the hatched area in Figure 16. This area provides us with a rough estimate of the systematic uncertainty we may have from mismatches between the actual telescope performance and the MC simulation (in case of a significant mismatch, tighter signal selection cuts always result in underestimated fluxes).

In view of the behavior of the low-energy spectral points, which lie significantly above the best-fit SED, we also evaluated the effect of a possible systematic error in the background estimation. The baseline assumption in the analysis is that the signal and the control regions have identical acceptance, and hence the event count in the latter is an unbiased estimate of the number of background events in the former. The open markers in Figure 16 show how the spectral points would change when the background estimate is increased by 1%. Such a small increase in the background, which only affects the lowest-energy part of the SED, is enough to bring the anomalous spectral points well below the best-fit SED and the Fermi-LAT measurements in the same energy range. This test highlights the limited background suppression capabilities of a single IACT near its threshold, resulting in gamma-ray excesses of only a few percent of the residual background, even for a source as bright as the Crab Nebula. Note that the large effect in the SED below 100 GeV of the 1% background modification actually hints at a smaller background systematic error, if we take the Fermi-LAT points as a reference. As a further check, we also compared the background rate after cuts in two off-source regions at the same distance from the center of the field of view ($0^\circ.4$), and equidistant from the Crab, and we obtain a difference between

Table 1

Spectral Parameters for the Source-independent and Source-dependent Analyses of the Crab Nebula in the Energy Range 50 GeV–30 TeV Assuming a Log-parabolic Parameterization

Analysis Type	f_0 ($\text{TeV}^{-1}\text{cm}^{-2}\text{s}^{-1}$)	E_0 (GeV)	α	β	χ^2 / N_{dof}
Source-independent	$(3.05 \pm 0.02) \times 10^{-10}$	400	2.25 ± 0.01	0.114 ± 0.006	48.5 / 18
Source-dependent	$(2.87 \pm 0.02) \times 10^{-10}$	400	2.26 ± 0.01	0.115 ± 0.006	32.9 / 18

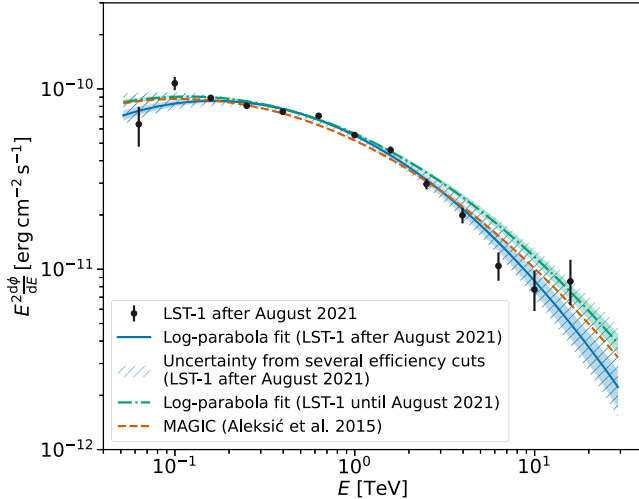


Figure 17. Comparison of Crab Nebula SED before and after the update of the LST-1 trigger settings in 2021 August, with 70% efficiency γ -ness and θ selection cuts. The image *intensity* cut is >80 p.e. before 2021 August, and >50 p.e. afterward (see the text). Spectral points are shown for the post-August sample only. The best fit to a log-parabola model and the corresponding statistical error bands for both data samples are also displayed. The hatched region represents the effect of varying the efficiency of the signal selection cuts for the data sample taken after 2021 August.

them of $0.5\% \pm 0.2\%$ (5557 ± 1534 events, for an average background of 1.18×10^6 events) for $E_{\text{reco}} < 63$ GeV. We cannot claim this to be the systematic uncertainty of the background estimation at low energies, valid for all LST-1 observations, since this is expected to depend on the camera response homogeneity, and hence on details like the brightness and distribution of stars in the field of view.

The obtained LST-1 Crab spectrum is very close (within 10% in flux) to the MAGIC reference (Aleksić et al. 2015). Considering the systematic uncertainties in both measurements, no significant discrepancies are seen. The spectrum also connects smoothly with the most energetic part of the Fermi-LAT spectrum (Arakawa et al. 2020), as illustrated by the joint fit of the Fermi-LAT and LST-1 SEDs to a log-parabola model shown in Figure 16. The observed bump in the SED is commonly explained by the inverse Compton emission. From the joint fit, we estimate the position of the peak to be around 60 GeV. We note that the resulting statistics from this fit would not be meaningful because only statistical uncertainties are considered, whereas the systematic uncertainties, very relevant especially near the threshold, are not taken into account.

Additionally, we evaluated the SEDs obtained with LST-1 before and after setting up the current trigger settings in 2021 August, which resulted in a lower and more stable energy threshold, as explained in Section 4. We split the data set into two samples corresponding to the observations carried out before and after 2021 August. The live times of the data sample until and after 2021 August are 25.4 hr and 8.8 hr, respectively. Both SEDs are compared in Figure 17. As there are fewer data

collected after 2021 August, we use five bins per decade to calculate the flux points. We note that the post-2021 August sample has a slightly lower flux, perhaps related to the lower average light collection efficiency estimated from muons (see Section 5). Moreover, this subset could be affected more significantly by external factors like nonoptimal atmospheric conditions, since its time interval is shorter. The agreement is better when soft cuts are applied (see the upper edge of the hashed blue band on Figure 17), which could point to a slightly worse agreement of data and MC for this data subset.

We remark that the bulk of the post-2021 August sample was recorded after the interruption of LST-1 operations due to the eruption of the Cumbre Vieja volcano in La Palma between 2021 September 19 and December 13.

6.2.1. Spectrum Obtained with the Source-dependent Analysis

We also computed the spectrum of the Crab Nebula using the source-dependent analysis to validate this analysis method. For this analysis, energy-dependent α cuts are applied to obtain a given gamma-ray efficiency, instead of the θ cut used in source-independent analysis. The right panel of Figure 16 shows the Crab Nebula SED obtained with source-dependent analysis for the whole data set, and a cut in *intensity* > 80 p.e. The flux points and best-fit models are computed with 70% efficiency cuts for both γ -ness and α . The best-fit model parameters are also indicated in Table 1. Although the flux of the best-fit model is statistically incompatible with that derived from the source-independent analysis, we must keep in mind that the uncertainties quoted in the table are just statistical. As in the source-independent analysis, event selection cuts are changed to obtain (40, 70, 90)% gamma-efficiency for γ -ness, and (70, 90)% in the case of α , as an estimate of the systematic uncertainty related to data–MC discrepancies. The result is represented as the hatched band in Figure 16. When these bands are considered, the SEDs from the source-dependent and the source-independent analyses are compatible.

Additionally, in the case of source-dependent analysis, the lowest-energy spectral points deviate significantly from the best-fit SED. But again, a subpercent variation of the background normalization would be enough to make them match the fit. Once more, we emphasize the importance of considering potential background systematic uncertainties in the spectral analysis of IACT data (eventually, this should be included in the likelihood maximization as a nuisance parameter). Note that this is a potential issue not only for single IACTs—even a stereoscopic system, with much stronger background suppression, can face a similar problem with dimmer sources in long-term observations.

6.2.2. Light Curve

In order to check the stability of the VHE gamma-ray flux from the Crab Nebula throughout the observations reported in this work ($\simeq 1.5$ yr), we calculated the daily light curve above 100 GeV, which is a safe minimum energy to avoid threshold

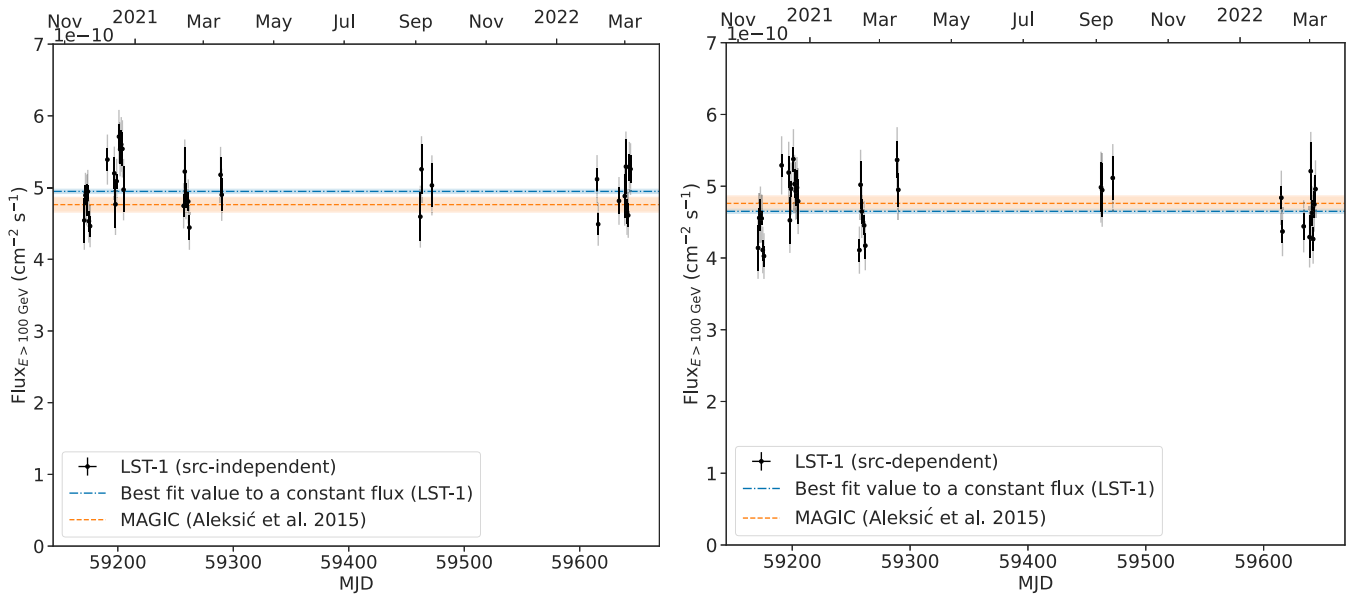


Figure 18. Crab Nebula light curve with 1 day bins above 100 GeV for source-independent (left) and source-dependent analyses (right). The dashed–dotted line is the best fit to a constant flux. We also indicate the integral flux in the same energy range calculated from the log-parabola model reported in Aleksić et al. (2015) with a dashed line. The black error bars correspond to the statistical errors. The gray bars include the systematic uncertainties (added in quadratic sum) assuming they are 6% and 7% of the flux values for source-independent and source-dependent analysis, respectively.

effects, and displayed it in Figure 18 for both analysis approaches. We assume a log-parabola spectral model with the corresponding best-fit parameters indicated in Table 1. Flux points are fitted to a constant value of

$$F_{>100\text{ GeV}} = (4.95 \pm 0.03) \times 10^{-10} \text{ cm}^{-2} \text{ s}^{-1}$$

with $\chi^2/N_{\text{dof}} = 119.2/33$ (P – value = 1×10^{-11})

for the source-independent analysis, and

$$F_{>100\text{ GeV}} = (4.65 \pm 0.03) \times 10^{-10} \text{ cm}^{-2} \text{ s}^{-1}$$

with $\chi^2/N_{\text{dof}} = 147.6/33$ (P – value = 2×10^{-16})

for the source-dependent analysis. Both results are, at face value, strongly incompatible with the (presumably) steady VHE flux of the nebula. However, only statistical uncertainties are considered—and from the tests performed with spectra (varying cut efficiencies and background normalization), it is clear that the total uncertainty must be significantly larger.

In order to obtain a light curve “fully compatible” with a steady flux (p -value $\simeq 0.5$), we have to assume, for the source-independent analysis, an additional systematic uncertainty of 6% on the nightly flux values, added in quadrature to the statistical uncertainty (see Figure 18). In the case of the source-dependent analysis, the value is 7%. This level of systematics seems plausible, considering that no run-wise or night-wise IRFs (to account for variable observation conditions or telescope performance) have been used in the calculations. Obviously, these estimates, computed under the assumption that the Crab Nebula flux is constant at these energies, do not tell us anything about a possible overall systematic error affecting all nights in the sample.

6.3. Crab Pulsar Phaseogram

The observations of the Crab Nebula have as byproduct another low-energy source that can be used to study its performance. The Crab pulsar (PSR J0534+220) is a young

neutron star with a rotational period of 33 ms created after the supernova explosion SN1054. It has the second-highest spin-down power known ($\dot{E} = 4.6 \times 10^{38} \text{ erg s}^{-1}$). It was first detected at VHE gamma rays by MAGIC (Aliu et al. 2008), and over the years its spectrum was extended up to teraelectronvolt energies (VERITAS Collaboration et al. 2011; Aleksić et al. 2012; Ansoldi et al. 2016). The data set used to search for pulsations is the same as in the rest of this article. The Crab pulsar phases definition is taken from Aleksić et al. (2012). Both P1 and P2 peaks are significantly detected as it can be seen in Figure 19, produced with the source-dependent analysis and fixed cuts ($\text{gammaness} > 0.6$, $\alpha < 12^\circ$). Calculation of the pulsar spectrum will require a more detailed treatment of the runs with nonstandard trigger threshold settings, and is a work in progress that will be the subject of a future publication.

7. Summary and Conclusions

We presented in this paper the observations of the Crab Nebula with the CTA LST-1 telescope performed during its commissioning period, and used them to evaluate the instrument performance in single-telescope mode.

The optical efficiency of the system, as determined with muon rings, is stable within $\pm 5\%$ in the $\simeq 1.5$ yr span of the data set shown in this paper. The trigger threshold, on the other hand, was not fully stable through this period, and is on average a little higher than its design value (reached only in 2021 August). The trigger threshold for the current configuration is 20 GeV, which increases to $\simeq 30$ GeV after analysis cuts.

The standard source-independent analysis can reach an angular resolution better than $0^\circ.12$ for $E > 1$ TeV using hard cuts (low efficiency). For the baseline cuts (70% efficiency) used to derive the spectra and light curves presented in this paper, the angular resolution is $\simeq 0^\circ.17$ for $E > 1$ TeV and $\simeq 0^\circ.34$ at $E = 100$ GeV. The energy resolution reaches the level of 20% for $E > 1$ TeV, and 35% at $E = 100$ GeV for low-zenith

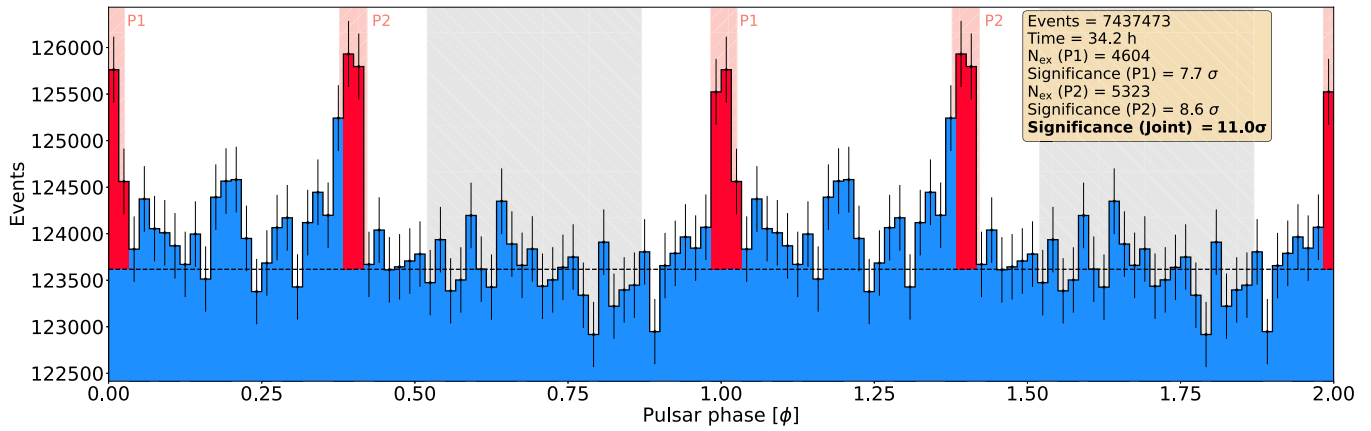


Figure 19. Crab pulsar phaseogram. The Crab pulsar phases definition is taken from Aleksić et al. (2012). We use the source-dependent analysis with fixed cuts for the whole energy range of $gammaness > 0.6$ and $\alpha < 12^\circ$ and $intensity > 50$ p.e.

observations. Below 50 GeV, the source-dependent analysis provides slightly better energy resolution and smaller bias.

In terms of flux sensitivity, the source-independent and source-dependent analyses provide similar performance, with the latter being slightly better at the highest energies. The 50 hr sensitivity above 100 GeV is about ~ 1.5 times worse than that of the MAGIC telescopes that operate in a similar energy range in stereoscopic mode. The advantages of stereoscopic reconstruction are, as expected, not overcome by the larger light collection efficiency of the LST-1 (from its larger dish and more efficient camera). The optimal 50 hr differential sensitivity achieved is $\sim 1.7\%$ C.U. at 800 GeV using source-independent analysis. The best integral sensitivity of the instrument is 1.1% C.U. above 250 GeV in 50 hr (12.4% C.U. in 0.5 hr).

We find that the Crab Nebula spectra derived using source-dependent and source-independent analysis are both very close (within 10%) to the spectrum determined with the MAGIC telescopes. The fact that the spectral fit results (obtained using only statistical uncertainties) from the two methods are not statistically compatible clearly indicates that for a bright source like the Crab Nebula, statistical uncertainties are subdominant with respect to systematics uncertainties, like those resulting from small data–MC discrepancies, or from inhomogeneities of the telescope response across the field of view, which may result in a biased background estimation.

We also find a smooth connection between the LST-1 spectrum and the Fermi-LAT one, especially when the possible systematics in the background normalization in the LST-1 near-threshold analysis are taken into account. The Crab Nebula night-wise light curves above 100 GeV derived using the two analyses are compatible with a steady emission if an additional systematic uncertainty in the flux values of $\simeq 7\%$ is assumed. Under the assumption that the VHE emission from the Crab Nebula was stable during the LST-1 observations, this again shows that systematic uncertainties in the calculated fluxes are nonnegligible in an observation like the one presented here, and should become the focus of future analysis improvements.

Acknowledgments

The Camera time-stamping hardware was developed and provided by the Astroparticle and Cosmology laboratory (APC at Université Paris Cité CNRS-IN2P3).

We gratefully acknowledge financial support from the following agencies and organizations:

Conselho Nacional de Desenvolvimento Científico e Tecnológico (CNPq), Fundação de Amparo à Pesquisa do Estado do Rio de Janeiro (FAPERJ), Fundação de Amparo à Pesquisa do Estado de São Paulo (FAPESP), Fundação de Apoio à Ciência, Tecnologia e Inovação do Paraná—Fundação Araucária, Ministry of Science, Technology, Innovations and Communications (MCTIC), Brasil; Ministry of Education and Science, National RI Roadmap Project DOI-153/28.08.2018, Bulgaria; Croatian Science Foundation, Rudjer Boskovic Institute, University of Osijek, University of Rijeka, University of Split, Faculty of Electrical Engineering, Mechanical Engineering and Naval Architecture, University of Zagreb, Faculty of Electrical Engineering and Computing, Croatia; Ministry of Education, Youth and Sports, MEYS LM2015046, LM2018105, LTT17006, EU/MEYS CZ.02.1.01/0.0/0.0/16_013/0001403, CZ.02.1.01/0.0/0.0/18_046/0016007 and CZ.02.1.01/0.0/0.0/16_019/0000754, Czech Republic; CNRS-IN2P3, the French Programme d’investissements d’avenir and the Enigmass Labex, This work has been done thanks to the facilities offered by the Univ. Savoie Mont Blanc—CNRS/IN2P3 MUST computing center, France; Max Planck Society, German Bundesministerium für Bildung und Forschung (Verbundforschung / ErUM), Deutsche Forschungsgemeinschaft (SFBs 876 and 1491), Germany; Istituto Nazionale di Astrofisica (INAF), Istituto Nazionale di Fisica Nucleare (INFN), Italian Ministry for University and Research (MUR); ICRR, University of Tokyo, JSPS, MEXT, Japan; JST SPRING—JPMJSP2108; Narodowe Centrum Nauki, grant No. 2019/34/E/ST9/00224, Poland. The Spanish groups acknowledge the Spanish Ministry of Science and Innovation and the Spanish Research State Agency (AEI) through the government budget lines PGE2021/28.06.000X.411.01, PGE2022/28.06.000X.411.01, and PGE2022/28.06.000X.711.04, and grants PID2022-139117NB-C44, PID2019-104114RB-C31, PID2019-107847RB-C44, PID2019-104114RB-C32, PID2019-105510GB-C31, PID2019-104114RB-C33, PID2019-107847RB-C41, PID2019-107847RB-C43, PID2019-107847RB-C42, PID2019-107988GB-C22, PID2021-124581OB-I00, PID2021-125331NB-I00; the “Centro de Excelencia Severo Ochoa” program through grant Nos. CEX2019-000920-S, CEX2020-001007-S, CEX2021-001131-S; the “Unidad de Excelencia María de Maeztu” program through grant Nos. CEX2019-000918-M, CEX2020-001058-M; the “Ramón y Cajal” program through grants RYC2021-032552-I, RYC2021-032991-I, RYC2020-

028639-I, and RYC-2017-22665; the “Juan de la Cierva-Incorporación” program through grant Nos. IJC2018-037195-I and IJC2019-040315-I. They also acknowledge the “Atracción de Talento” program of Comunidad de Madrid through grant No. 2019-T2/TIC-12900; the project “Tecnologías avanzadas para la exploración del universo y sus componentes” (PR47/21 TAU), funded by Comunidad de Madrid, by the Recovery, Transformation and Resilience Plan from the Spanish State, and by NextGenerationEU from the European Union through the Recovery and Resilience Facility; the La Caixa Banking Foundation, grant No. LCF/BQ/PI21/11830030; the “Programa Operativo” FEDER 2014-2020, Consejería de Economía y Conocimiento de la Junta de Andalucía (Ref. 1257737), PAIDI 2020 (Ref. P18-FR-1580) and Universidad de Jaén; “Programa Operativo de Crecimiento Inteligente” FEDER 2014-2020 (Ref. ESFRI-2017-IAC-12), Ministerio de Ciencia e Innovación, 15% co-financed by Consejería de Economía, Industria, Comercio y Conocimiento del Gobierno de Canarias; the “CERCA” program and the grant 2021SGR00426, both funded by the Generalitat de Catalunya; and the European Union’s “Horizon 2020” GA:824064 and NextGenerationEU (PRTR-C17.I1). State Secretariat for Education, Research and Innovation (SERI) and Swiss National Science Foundation (SNSF), Switzerland; The research leading to these results has received funding from the European Union’s Seventh Framework Programme (FP7/2007-2013) under grant agreement Nos. 262053 and No 317446. This project is receiving funding from the European Union’s Horizon 2020 research and innovation programs under agreement No. 676134. ESCAPE (The European Science Cluster of Astronomy & Particle Physics ESFRI Research Infrastructures) has received funding from the European Union’s Horizon 2020 research and innovation program under grant agreement No. 824064.

Software: The analysis and figures of this manuscript were produced using the following open-access software tools: Astropy (Astropy Collaboration et al. 2013, 2018), Matplotlib (Hunter 2007), NumPy (van der Walt et al. 2011), Scikit-learn (Pedregosa et al. 2011) and SciPy (Virtanen et al. 2020). All numerical data of the figures in the paper, and scripts to reproduce them, are available at Lopez-Coto et al. (2023).

Author Contribution

This paper has gone through internal review by the CTA Consortium.

R. López-Coto: project coordination, muon ring analysis, sensitivity estimation, Crab pulsar analysis. A. Moralejo: project coordination, data sample selection, data-MC cross-validation, sensitivity estimation. D. Morcuende: data analysis, Crab Nebula spectrum and light curve (source-independent approach). S. Nozaki: data analysis, Crab Nebula spectrum and light curve (source-dependent approach). T. Vuillaume: Monte Carlo processing, Random Forest generation, computation of the instrument response functions. All five corresponding authors above have participated in the paper drafting and edition. The rest of the authors have contributed in one or several of the following ways: design, construction, maintenance, and operation of the instrument(s) used to acquire the data; preparation and/or evaluation of the observation proposals; data acquisition, processing, calibration and/or reduction; production of analysis tools and/or related Monte Carlo simulations; discussion and approval of the contents of the draft.

Appendix

A.1. Random Forests Features

The parameters used to train the random forest models are listed below (see also Figure 3):

1. *log_intensity*: decimal logarithm of *intensity*, the sum of the charges (in photoelectrons) of the pixels that survive the image cleaning. All other image parameters listed below are calculated using the same set of pixels.
2. *width*, *length*: width and length of the ellipsoid, i.e., the second-order moments of the charge distribution along the minor and major axes of the image.
3. *wl*: width over length ratio
4. *x*, *y*: coordinates of the image centroid (first order moments) in the camera frame
5. *skewness*: skewness of the image
6. *kurtosis*: kurtosis of the image
7. *time_gradient*: gradient of the signal arrival times, computed along the main axis of the image
8. *leakage_intensity_width_2*: fraction of the total charge of the image that is recorded on pixels at the edge of the camera, or their next neighbors.
9. *az_tel*, *alt_tel*: telescope pointing direction (azimuth and altitude, respectively)
10. *disp_norm*: distance between (*x,y*) and the point along the major image axis that is closest to the true (nominal) source position.
11. *disp_sign*: indicates on which side of the image centroid (*x,y*) the true source position lies.
12. *dist*: distance between (*x,y*) and the true (nominal) source position on the camera.
13. *reco_disp_norm_diff*: $\text{abs}(\text{dist} - \text{reco_disp_norm})$
14. *reco_disp_sign_correctness*: estimated probability (obtained from the *disp_sign* random forest using the `predict_proba` method of `scikit-learn`) that the known source position (on either side of the centroid along the major axis) is the correct one for the given image.

A.2. Random Forest Hyperparameters








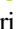










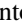





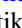



























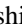



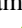


The random forest regressors (for the energy and disp. reconstruction) are trained using `scikit-learn` v1.0 with the following hyperparameters:

1. `max_depth = 30`
2. `min_sample_leaf = 10`
3. `n_estimators = 150`
4. `max_depth = true`
5. `criterion = squared_error`
6. `max_features = auto`
7. `max_leaf_nodes = null`
8. `min_impurity_decrease = 0.0`
9. `min_samples_split = 10`
10. `min_weight_fraction_leaf = 0.0`

The classifier uses the same parameters, with the following differences: `n_estimators = 100`, `criterion = gini`. Notably, the `max_depth`, `n_estimators`, `min_sample_leaf`, and `min_sample_split` parameter values have been optimized using a grid search to minimize computing resources without compromising the models performances.

ORCID iDs

- I. Agudo  <https://orcid.org/0000-0002-3777-6182>
 L. A. Antonelli  <https://orcid.org/0000-0002-5037-9034>
 C. Aramo  <https://orcid.org/0000-0002-8412-3846>
 M. Artero  <https://orcid.org/0000-0002-4899-8127>
 K. Asano  <https://orcid.org/0000-0001-9064-160X>
 A. Baktash  <https://orcid.org/0000-0002-5439-117X>
 A. Bamba  <https://orcid.org/0000-0003-0890-4920>
 A. Baquero Larriva  <https://orcid.org/0000-0002-1757-5826>
 L. Baroncelli  <https://orcid.org/0000-0002-9215-4992>
 U. Barres de Almeida  <https://orcid.org/0000-0001-7909-588X>
 J. A. Barrio  <https://orcid.org/0000-0002-0965-0259>
 I. Batkovic  <https://orcid.org/0000-0002-1209-2542>
 J. Becerra González  <https://orcid.org/0000-0002-6729-9022>
 E. Bernardini  <https://orcid.org/0000-0003-3108-1141>
 A. Berti  <https://orcid.org/0000-0003-0396-4190>
 N. Biederbeck  <https://orcid.org/0000-0003-3708-9785>
 C. Bigongiari  <https://orcid.org/0000-0003-3293-8522>
 E. Bissaldi  <https://orcid.org/0000-0001-9935-8106>
 O. Blanch  <https://orcid.org/0000-0002-8380-1633>
 P. Bordas  <https://orcid.org/0000-0002-0266-8536>
 A. Bulgarelli  <https://orcid.org/0000-0001-6347-0649>
 M. Buscemi  <https://orcid.org/0000-0003-2123-5434>
 M. Cardillo  <https://orcid.org/0000-0001-8877-3996>
 S. Caroff  <https://orcid.org/0000-0002-1103-130X>
 A. Carosi  <https://orcid.org/0000-0001-8690-6804>
 F. Cassol  <https://orcid.org/0000-0002-0372-1992>
 Y. Chai  <https://orcid.org/0000-0003-2816-2821>
 J. L. Contreras  <https://orcid.org/0000-0001-7282-2394>
 J. Cortina  <https://orcid.org/0000-0003-4576-0452>
 H. Costantini  <https://orcid.org/0000-0003-4027-3081>
 A. De Angelis  <https://orcid.org/0000-0002-3288-2517>
 M. de Bony de Lavergne  <https://orcid.org/0000-0002-4650-1666>
 C. Delgado  <https://orcid.org/0000-0002-7014-4101>
 J. Delgado Mengual  <https://orcid.org/0000-0002-0166-5464>
 D. della Volpe  <https://orcid.org/0000-0001-8530-7447>
 F. Di Piero  <https://orcid.org/0000-0003-4861-432X>
 L. Di Venere  <https://orcid.org/0000-0003-0703-824X>
 C. Díaz  <https://orcid.org/0000-0002-5931-2709>
 R. M. Dominik  <https://orcid.org/0000-0003-4168-7200>
 D. Dominis Prester  <https://orcid.org/0000-0002-9880-5039>
 A. Donini  <https://orcid.org/0000-0002-3066-724X>
 D. Dorner  <https://orcid.org/0000-0001-8823-479X>
 M. Doro  <https://orcid.org/0000-0001-9104-3214>
 D. Elsässer  <https://orcid.org/0000-0001-6796-3205>
 G. Emery  <https://orcid.org/0000-0001-6155-4742>
 J. Escudero  <https://orcid.org/0000-0002-4131-655X>
 A. Fiasson  <https://orcid.org/0000-0002-4209-6157>
 L. Freixas Coromina  <https://orcid.org/0000-0002-2015-9823>
 S. Fukami  <https://orcid.org/0000-0003-4025-7794>
 Y. Fukazawa  <https://orcid.org/0000-0002-0921-8837>
 E. Garcia  <https://orcid.org/0000-0003-2224-4594>
 R. Garcia López  <https://orcid.org/0000-0002-8204-6832>
 D. Gasparri  <https://orcid.org/0000-0002-5064-9495>
 N. Giglietto  <https://orcid.org/0000-0002-9021-2888>
 F. Giordano  <https://orcid.org/0000-0002-8651-2394>
 P. Gliwny  <https://orcid.org/0000-0002-4183-391X>
 N. Godinovic  <https://orcid.org/0000-0002-4674-9450>
 D. Green  <https://orcid.org/0000-0003-0768-2203>
 J. Green  <https://orcid.org/0000-0002-1130-6692>
 S. Gunji  <https://orcid.org/0000-0002-5881-2445>
 D. Hadasch  <https://orcid.org/0000-0001-8663-6461>
 A. Hahn  <https://orcid.org/0000-0003-0827-5642>
 T. Hassan  <https://orcid.org/0000-0002-4758-9196>
 K. Hayashi  <https://orcid.org/0000-0002-8758-8139>
 L. Heckmann  <https://orcid.org/0000-0002-6653-8407>
 M. Heller  <https://orcid.org/0000-0003-1215-0148>
 J. Herrera Llorente  <https://orcid.org/0000-0002-3771-4918>
 K. Hirofani  <https://orcid.org/0000-0002-2472-9002>
 D. Hoffmann  <https://orcid.org/0000-0001-5209-5265>
 D. Horns  <https://orcid.org/0000-0003-1945-0119>
 J. Houles  <https://orcid.org/0000-0002-5373-7992>
 M. Hrabovsky  <https://orcid.org/0000-0003-4223-7316>
 D. Hrupec  <https://orcid.org/0000-0002-7027-5021>
 M. Hütten  <https://orcid.org/0000-0002-2133-5251>
 R. Imazawa  <https://orcid.org/0000-0002-0643-7946>
 T. Inada  <https://orcid.org/0000-0002-6923-9314>
 Y. Inome  <https://orcid.org/0000-0002-3517-1956>
 M. Iori  <https://orcid.org/0000-0002-1302-9094>
 M. Jacquemont  <https://orcid.org/0000-0002-4012-6930>
 I. Jimenez Martinez  <https://orcid.org/0000-0003-2150-6919>
 J. Jurysek  <https://orcid.org/0000-0002-3130-4168>
 V. Karas  <https://orcid.org/0000-0002-5760-0459>
 H. Katagiri  <https://orcid.org/0000-0003-2347-8819>
 J. Kataoka  <https://orcid.org/0000-0003-2819-6415>
 D. Kerszberg  <https://orcid.org/0000-0002-5289-1509>
 Y. Kobayashi  <https://orcid.org/0000-0001-5551-2845>
 A. Kong  <https://orcid.org/0000-0002-5105-344X>
 H. Kubo  <https://orcid.org/0000-0001-9159-9853>
 J. Kushida  <https://orcid.org/0000-0002-8002-8585>
 A. Lamastra  <https://orcid.org/0000-0003-2403-913X>
 M. Linhoff  <https://orcid.org/0000-0001-7993-8189>
 F. Longo  <https://orcid.org/0000-0003-2501-2270>
 R. López-Coto  <https://orcid.org/0000-0002-3882-9477>
 M. López-Moya  <https://orcid.org/0000-0002-8791-7908>
 A. López-Oramas  <https://orcid.org/0000-0003-4603-1884>
 P. L. Luque-Escamilla  <https://orcid.org/0000-0002-3306-9456>
 P. Majumdar  <https://orcid.org/0000-0002-5481-5040>
 M. Makariev  <https://orcid.org/0000-0002-1622-3116>
 D. Mandat  <https://orcid.org/0000-0001-7748-7468>
 M. Manganaro  <https://orcid.org/0000-0003-1530-3031>
 K. Mannheim  <https://orcid.org/0000-0002-2950-6641>
 M. Mariotti  <https://orcid.org/0000-0003-3297-4128>
 P. Marquez  <https://orcid.org/0000-0002-9591-7967>
 G. Marsella  <https://orcid.org/0000-0002-3152-8874>
 J. Martí  <https://orcid.org/0000-0001-5302-0660>
 O. Martinez  <https://orcid.org/0000-0001-9052-856X>
 G. Martínez  <https://orcid.org/0000-0002-1061-8520>
 M. Martínez  <https://orcid.org/0000-0002-9763-9155>
 P. Marusevec  <https://orcid.org/0000-0002-6748-4615>
 A. Mas-Aguilar  <https://orcid.org/0000-0002-8893-9009>
 G. Maurin  <https://orcid.org/0000-0002-6970-0588>
 D. Mazin  <https://orcid.org/0000-0002-2010-4005>
 S. Micanovic  <https://orcid.org/0000-0002-0076-3134>
 D. Miceli  <https://orcid.org/0000-0002-2686-0098>
 T. Miener  <https://orcid.org/0000-0003-1821-7964>
 J. M. Miranda  <https://orcid.org/0000-0002-1472-9690>
 R. Mirzoyan  <https://orcid.org/0000-0003-0163-7233>

T. Mizuno  <https://orcid.org/0000-0001-7263-0296>
 E. Molina  <https://orcid.org/0000-0003-1204-5516>
 T. Montaruli  <https://orcid.org/0000-0001-5014-2152>
 A. Moralejo  <https://orcid.org/0000-0002-1344-9080>
 D. Morcuende  <https://orcid.org/0000-0001-9400-0922>
 A. Morselli  <https://orcid.org/0000-0002-7704-9553>
 K. Murase  <https://orcid.org/0000-0002-5358-5642>
 T. Nakamori  <https://orcid.org/0000-0002-7308-2356>
 L. Nickel  <https://orcid.org/0000-0001-7110-0533>
 M. Nievas  <https://orcid.org/0000-0002-8321-9168>
 K. Nishijima  <https://orcid.org/0000-0002-1830-4251>
 K. Noda  <https://orcid.org/0000-0003-1397-6478>
 D. Nosek  <https://orcid.org/0000-0001-6219-200X>
 S. Nozaki  <https://orcid.org/0000-0002-6246-2767>
 M. Ohishi  <https://orcid.org/0000-0003-2775-7487>
 Y. Ohtani  <https://orcid.org/0000-0001-7042-4958>
 A. Okumura  <https://orcid.org/0000-0002-3055-7964>
 J. Otero-Santos  <https://orcid.org/0000-0002-4241-5875>
 M. Palatiello  <https://orcid.org/0000-0002-4124-5747>
 D. Paneque  <https://orcid.org/0000-0002-2830-0502>
 R. Paoletti  <https://orcid.org/0000-0003-0158-2826>
 J. M. Paredes  <https://orcid.org/0000-0002-1566-9044>
 M. Pech  <https://orcid.org/0000-0002-8421-0456>
 M. Pecimotika  <https://orcid.org/0000-0002-4699-1845>
 V. Poireau  <https://orcid.org/0000-0002-4768-0256>
 E. Prandini  <https://orcid.org/0000-0003-4502-9053>
 J. Prast  <https://orcid.org/0000-0002-6926-9871>
 C. Priyadarshi  <https://orcid.org/0000-0002-9160-9617>
 R. Rando  <https://orcid.org/0000-0001-6992-818X>
 W. Rhode  <https://orcid.org/0000-0003-2636-5000>
 M. Ribó  <https://orcid.org/0000-0002-9931-4557>
 V. Rizi  <https://orcid.org/0000-0002-5277-6527>
 T. Saito  <https://orcid.org/0000-0001-6201-3761>
 S. Sakurai  <https://orcid.org/0000-0001-7427-4520>
 T. Šarić  <https://orcid.org/0000-0001-8731-8369>
 F. G. Saturni  <https://orcid.org/0000-0002-1946-7706>
 B. Schleicher  <https://orcid.org/0000-0001-8624-8629>
 F. Schussler  <https://orcid.org/0000-0003-1500-6571>
 M. Seglar Arroyo  <https://orcid.org/0000-0001-8654-409X>
 J. Sitarek  <https://orcid.org/0000-0002-1659-5374>
 V. Sliusar  <https://orcid.org/0000-0002-4387-9372>
 A. Spolon  <https://orcid.org/0000-0001-8770-9503>
 J. Strišćković  <https://orcid.org/0000-0003-2902-5044>
 M. Strzys  <https://orcid.org/0000-0001-5049-1045>
 Y. Suda  <https://orcid.org/0000-0002-2692-5891>
 Y. Sunada  <https://orcid.org/0000-0001-8629-5214>
 H. Tajima  <https://orcid.org/0000-0002-1721-7252>
 M. Takahashi  <https://orcid.org/0000-0002-0574-6018>
 J. Takata  <https://orcid.org/0000-0002-8731-0129>
 R. Takeishi  <https://orcid.org/0000-0001-6335-5317>
 P. H. T. Tam  <https://orcid.org/0000-0002-1262-7375>
 S. J. Tanaka  <https://orcid.org/0000-0002-8796-1992>
 D. Tateishi  <https://orcid.org/0000-0003-0248-4064>
 P. Temnikov  <https://orcid.org/0000-0002-9559-3384>
 Y. Terada  <https://orcid.org/0000-0002-2359-1857>
 T. Terzic  <https://orcid.org/0000-0002-4209-3407>
 D. F. Torres  <https://orcid.org/0000-0002-1522-9065>
 P. Travnicek  <https://orcid.org/0000-0002-1655-9584>
 M. Vacula  <https://orcid.org/0000-0003-4844-3962>

J. van Scherpenberg  <https://orcid.org/0000-0002-6173-867X>
 M. Vázquez Acosta  <https://orcid.org/0000-0002-2409-9792>
 V. Verguilov  <https://orcid.org/0000-0001-7911-1093>
 I. Viale  <https://orcid.org/0000-0001-5031-5930>
 C. F. Vigorito  <https://orcid.org/0000-0002-0069-9195>
 V. Vitale  <https://orcid.org/0000-0001-8040-7852>
 I. Vovk  <https://orcid.org/0000-0003-3444-3830>
 T. Vuillaume  <https://orcid.org/0000-0002-5686-2078>
 M. Will  <https://orcid.org/0000-0002-7504-2083>
 T. Yamamoto  <https://orcid.org/0000-0001-9734-8203>
 R. Yamazaki  <https://orcid.org/0000-0002-1251-7889>
 T. Yoshida  <https://orcid.org/0000-0002-7708-6362>
 T. Yoshikoshi  <https://orcid.org/0000-0002-6045-9839>
 N. Zywucka  <https://orcid.org/0000-0003-2644-6441>
 K. Bernlöhner  <https://orcid.org/0000-0001-8065-3252>
 O. Gueta  <https://orcid.org/0000-0002-9440-2398>
 K. Kosack  <https://orcid.org/0000-0001-8424-3621>
 G. Maier  <https://orcid.org/0000-0001-9868-4700>
 J. Watson  <https://orcid.org/0000-0003-4282-7463>

References

- Abdo, A. A., Ackermann, M., Ajello, M., et al. 2011, *Sci*, 331, 739
 Acero, F., Ackermann, M., Ajello, M., et al. 2015, *ApJS*, 218, 23
 Aharonian, F., Akhperjanian, A. G., Bazer-Bachi, A. R., et al. 2006, *A&A*, 457, 899
 Aleksić, J., Alvarez, E. A., Antonelli, L. A., et al. 2012, *A&A*, 540, A69
 Aleksić, J., Ansoldi, S., Antonelli, L., et al. 2016, *Aph*, 72, 76
 Aleksić, J., Ansoldi, S., Antonelli, L. A., et al. 2015, *JHEAp*, 5, 30
 Aliu, E., Anderhub, H., Antonelli, L. A., et al. 2008, *Sci*, 322, 1221
 Aliu, E., Anderhub, H., Antonelli, L. A., et al. 2009, *Aph*, 30, 293
 Aliu, E., Archambault, S., Aune, T., et al. 2014, *ApJL*, 781, L11
 Ansoldi, S., Antonelli, L. A., Antoranz, P., et al. 2016, *A&A*, 585, A133
 Arakawa, M., Hayashida, M., Khangulyan, D., & Uchiyama, Y. 2020, *ApJ*, 897, 33
 Astropy Collaboration, Price-Whelan, A. M., Sipőcz, B. M., et al. 2018, *AJ*, 156, 123
 Astropy Collaboration, Robitaille, T. P., Tollerud, E. J., et al. 2013, *A&A*, 558, A33
 Bernlöhner, K. 2008, *Aph*, 30, 149
 Breiman, L. 2001, *Mach. Learn.*, 45, 5
 Breiman, L., Friedman, J., Olshen, R., & Stone, C. 1984, *Classification and Regression Trees* (London: Chapman and Hall/CRC)
 Bühler, R., & Blandford, R. 2014, *RPPH*, 77, 066901
 Cortina, J. 2019, *ICRC (Madison, WI)*, 36, 653
 Deil, C., Wood, M., Hassan, T., et al. 2018, *Data Formats for Gamma-ray Astronomy—version 0.2*, Zenodo, doi:10.5281/zenodo.1409831
 Deil, C., Zanin, R., Lefaucheur, J., et al. 2017, *ICRC (Busan)*, 301, 766
 Donath, A., Deil, C., Terrier, R., et al. 2022, *GammaPy: Python Toolbox for Gamma-ray Astronomy*, v0.20, Zenodo, doi:10.5281/zenodo.6552377
 Fomin, V., Stepanian, A., Lamb, R., et al. 1994, *Aph*, 2, 137
 García, E., Vuillaume, T., & Nickel, L. 2022, arXiv:2212.00120
 Gaug, M., Fegan, S., Mitchell, A. M. W., et al. 2019, *ApJS*, 243, 11
 Heck, D., Knapp, J., Capdevielle, J. N., Schatz, G., & Thouw, T. 1998, *CORSIKA: a Monte Carlo Code to Simulate Extensive Air Showers* FZKA 6019, Institute for Nuclear Physics, Forschungszentrum und Universität Karlsruhe, <https://www.iap.kit.edu/corsika/70.php>
 H.E.S.S. Collaboration 2020, *NatAs*, 4, 167
 H.E.S.S. Collaboration, Abramowski, A., Aharonian, F., et al. 2014, *A&A*, 562, L4
 Hester, J. J. 2008, *ARA&A*, 46, 127
 Hillas, A. M. 1985, *ICRC (OG Sessions)*, 3, 445
 Hunter, J. D. 2007, *CSE*, 9, 90
 Kobayashi, Y., Okumura, A., Cassol, F., et al. 2022, *ICRC (Berlin)*, 395, 720
 Kosack, K., Watson, J., Nöthe, M., et al. 2021, *cta-observatory/ctapipe: v0.12.0*, v0.12.0, Zenodo, doi:10.5281/zenodo.5720333
 Lessard, R., Buckley, J., Connaughton, V., & Le Bohec, S. 2001, *Aph*, 15, 1
 LHAASO Collaboration, Cao, Z., Aharonian, F., et al. 2021, *Sci*, 373, 425

- Lopez Coto, R., Moralejo Olaizola, A., Morcuende, D., Nozaki, S., & Vuillaume, T. 2023, Observations of the Crab Nebula and Pulsar with the Large-Sized Telescope prototype of the Cherenkov Telescope Array Data Points, v1.0.0, Zenodo, doi:[10.5281/zenodo.8159146](https://doi.org/10.5281/zenodo.8159146)
- Lopez-Coto, R., Vuillaume, T., Moralejo, A., et al. 2022, cta-observatory/cta-1stchain: v0.9.4, v0.9.4, Zenodo, doi:[10.5281/zenodo.6344674](https://doi.org/10.5281/zenodo.6344674)
- Morcuende, D., Ruiz, J. E., Saha, L., et al. 2022, cta-observatory/Istosa: v0.9.4, v0.9.4, Zenodo, doi:[10.5281/zenodo.6567234](https://doi.org/10.5281/zenodo.6567234)
- Nigro, C., Deil, C., Zanin, R., et al. 2019, *A&A*, **625**, A10
- Noethe, M., Kosack, K., Nickel, L., & Peresano, M. 2022, *ICRC (Berlin)*, **395**, 744
- Nöthe, M., Peresano, M., Sitarek, J., et al. 2022, cta-observatory/pyirf: v0.6.0—2022-01-10, v0.6.0, Zenodo, doi:[10.5281/zenodo.5833284](https://doi.org/10.5281/zenodo.5833284)
- Ohishi, M., Arbeletche, L., de Souza, V., et al. 2021, *JPhG*, **48**, 075201
- Pedregosa, F., Varoquaux, G., Gramfort, A., et al. 2011, *JMLR*, **12**, 2825
- Ruiz, J. E., Morcuende, D., Saha, L., et al. 2022, in ASP Conf. Ser. 532, *Astronomical Data Analysis Software and Systems XXX*, ed. J. E. Ruiz, F. Pierfederici, & P. Teuben (San Francisco, CA: ASP), 369
- Sitarek, J. 2022, *Galax*, **10**, 21
- van der Walt, S., Colbert, S. C., & Varoquaux, G. 2011, *CSE*, **13**, 22
- VERITAS Collaboration, Aliu, E., Arlen, T., et al. 2011, *Sci*, **334**, 69
- Virtanen, P., Gommers, R., Oliphant, T. E., et al. 2020, *NatMe*, **17**, 261
- Vuillaume, T., Garcia, E., & Nickel, L. 2022, Istmcpipe, v0.9.0, Zenodo, doi:[10.5281/zenodo.7180216](https://doi.org/10.5281/zenodo.7180216)
- Weekes, T. C., Cawley, M. F., Fegan, D. J., et al. 1989, *ApJ*, **342**, 379